

UNIVERSITY OF CALIFORNIA

Santa Barbara

Spatial Variability of Saturated Hydraulic Conductivity and Thresholds for Slope Failure at  
Sedgwick Ranch, California

A Thesis submitted in partial satisfaction of the  
requirements for the degree Master of Science  
in Earth Science

by

Paul A. Alessio

Committee in charge:

Professor Edward A. Keller, Chair

Professor Thomas Dunne

Professor Oliver A. Chadwick

September 2016

The thesis of Paul A. Alessio is approved.

---

Thomas Dunne

---

Oliver A. Chadwick

---

Edward A. Keller, Committee Chair

September 2016

Spatial Variability of Saturated Hydraulic Conductivity and Thresholds for Slope Failure at  
Sedgwick Ranch, California

Copyright © 2016

by

Paul A. Alessio

## ACKNOWLEDGEMENTS

I would like to express much appreciation to my advisor Ed Keller, whose encouragement and guidance have helped shape my goals and confidence in research. His attitude, energy, and dedication to science and his students are unparalleled, as is his passion for developing new ideas and creative solutions in the field geomorphology.

I would also like to extend my gratitude to my committee members Oliver Chadwick and Tom Dunne for their support as well as providing guidance and creative freedom with this project.

Thanks to Ron Pike at Pacific Soils for use of the lab.

This thesis is dedicated to my family, for their unconditional love and support.

See them tumbling down

Pledging their love to the ground

Humble and free I'll be found

Drifting along where hillsides fall down

## ABSTRACT

### Spatial Variability of Saturated Hydraulic Conductivity and Thresholds for Slope Failure at Sedgwick Ranch, California

by

Paul A. Alessio

Shallow landslides are commonly triggered by positive pore-fluid pressures linked to heavy rainfall. Positive pore-fluid pressures are generated at low-conductivity layers that occur within the soil profile or at the soil-bedrock interface. In this study, *in situ* measurements of saturated hydraulic conductivity ( $K_{\text{sat}}$ ) were performed at three historic debris flow sites to determine its variability and implications for triggering debris flows at Sedgwick Reserve, California. Falling head tests were performed in the soil column within each horizon and at the soil-bedrock interface to estimate  $K_{\text{sat}}$ . It was found that the failure plane exhibited  $K_{\text{sat}}$  values ranging from 4 to 33 mm/hr, whereas overlying soils of the A and B/Bt horizons exhibited higher infiltration rates, ranging from 37-138 mm/hr and 24-127 mm/hr, respectively. Below the failure plane,  $K_{\text{sat}}$  ranged from 4 to 120 mm/hr, signifying a pattern of fast-slow-fast infiltration. Measurements of grain size distributions and bulk density do not provide insight into the cause of low-conductivity at the soil-bedrock interface. Rather, field observations suggest that the infilling of fractures with fine-grained particles at the soil-bedrock interface may be the cause of the low-conductivity layer. Statistical analyses also show that  $K_{\text{sat}}$  has a strong dependence on soil horizon. Hillslope parameters and measurements of soil mechanical properties were used in a finite

slope-stability model to predict thresholds for failure. Results of the stability analysis predict failure at 35-50% saturation of the soil column above the failure plane. This study suggests that the vertical patterns and spatial variability in hydraulic conductivities of landslide-prone soils are important factors in predicting slope stability.

## TABLE OF CONTENTS

### I. Introduction

### II. Landslide Thresholds: Using Empirical Data, Maps, and Models

#### A. Previous Work on Debris Flows and $K_{sat}$

### III. Overview and Objectives

#### A. Landslide Warning Systems

#### B. Landform Evolution and Sediment Delivery

#### C. Study Site

#### D. Climate

#### E. Precipitation during the 1997-98' El Nino

#### F. Landsliding at Sedgwick Reserve

#### G. Soil-Water Dynamics at Sedgwick

### IV. Methods

#### A. Selection of Landslide Sites

#### B. Landslide and Soil Morphological Descriptions

#### C. Estimating $K_{sat}$

D. Grain size Analysis

E. Bulk Density

F. Shear Tests

G. Modeling Conditions for Failure

H. Analysis of Infiltration Data

## V. Results

A. Stability Analysis

B. Site Characterization and Field Observations

C. Site 1

D. Site 2

E. Site 3

F. Ksat Measurements

G. Kolmogorov-Smirnov tests

H. Direct Shear Tests

I. Grain Size

## VI. Discussion

A. Stability Analysis

B. Infiltration Measurements and Implications for Hillslope Stability

C. Failure Plane Formation

D. Failure Sites and Recurrence Intervals

## VII. Conclusions

## References

## Appendix

A. Table 3.1: Soil and Bedrock Characteristics for Site 1

B. Table 3.2: Soil and Bedrock Characteristics for Site 2

C. Table 3.3: Soil and Bedrock Characteristics for Site 3

## LIST OF FIGURES

Figure 1: A conceptual cross section of a hillslope, portraying conditions that may lead to debris flow initiation

Figure 2: Map displaying Santa Barbara County and Sedgwick Reserve, CA

Figure 3: Visualization of an atmospheric river over the Pacific Ocean striking the coast of southern California

Figure 4: Daily rainfall totals from the Figueroa Mountain Ranger Station

Figure 5: The falling-head single-ring infiltrometer used to make Ksat measurements

Figure 6: Stability curves for sites 1, 2, and 3

Figure 7: Sites 1,2, and 3 with infiltration measurements and pit locations marked

Figure 8: Stratigraphic columns for sites 1, 2 and 3 with soil descriptions and Paso Robles formation at the failure plane for site 3

Figure 9: Graph of Ksat vs. depth for sites 1, 2, and 3

Figure 10: Histograms showing the frequency and distribution of Ksat in the A and B horizons and the failure plane

Figure 11: Direct shear measurements for sites 1, 2, and 3

## **I. Introduction**

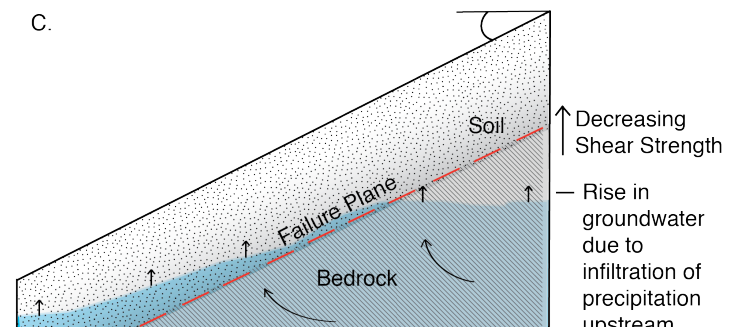
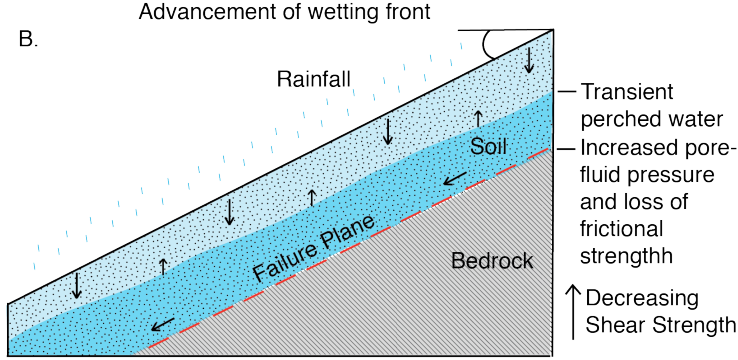
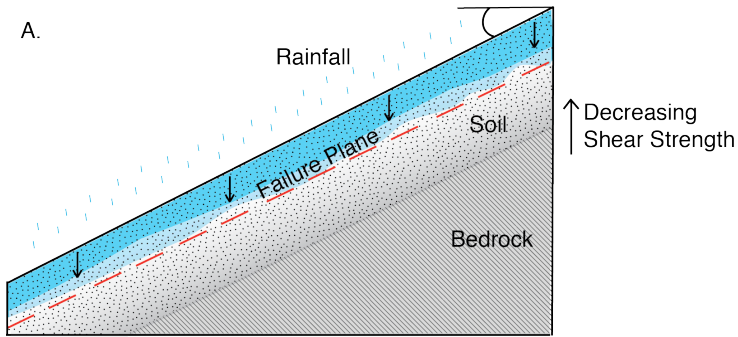
The California Coast Ranges experience intense, long-duration rainstorms that can trigger sudden shallow slope failures which evolve into debris flows capable of destroying buildings and infrastructure (Ellen and Wieczorek 1988; Wilson and Wieczorek, 1995; NOAA-USGS Debris-Flow Task force, 2005).

In Southern California, Campbell (1975) observed that circa 250 mm of antecedent seasonal rainfall were needed to saturate the soil mantle, such that subsequent storms may trigger landslides. Since then, similar studies have concluded that soil depth and hydraulic conductivity of the soil mantle are the most important factors in determining the amount of antecedent and storm-total rainfall needed to reach field saturation (Wilson and Wieczorek, 1995; Van Asch et al. 1999; Iverson, 2000). Furthermore, it is recognized that soil mantle thickness and hydrologic properties are especially sensitive parameters in hydrologic models (Sorbino, 2010).

Many shallow landslides fail by shear on a planar surface that is parallel to slope. From a hydrologic perspective, there are several conditions that facilitate landsliding: these include an increase in pore fluid pressure on a discontinuity surface, the advancement of the wetting front, and a rise in groundwater (Figure 1). Most shallow slope failures may initiate on a low permeability discontinuity surface when infiltration of water from heavy rainfall causes a rise in piezometric head, resulting in a loss of frictional strength (Campbell 1975; Sidle and Swanston 1982; Pradel 1993; Wilson and Wieczorek 1995; Van Asch 1998; Crozier, 1999; Iverson, 2000; Godt and McKenna 2008; Baum 2010). If a low conductivity layer is not present, the advancement of the wetting front alone may cause a loss of frictional strength and initiate debris flows (Matsushi, 2006). The rise in groundwater, resulting in

exfiltration through fractured bedrock may also initiate failure (Montgomery and Schmidt, 2009). It is also known that colluvial hollows or zero order basins: concave bedrock depressions on a hillslope that aren't occupied by channels, pose an increased susceptibility for landsliding due to their increased sedimentation and subsurface-flow accumulation (Dietrich and Dunne 1978; Reneau and Dietrich, 1986). In all of these cases, field-saturated hydraulic conductivity ( $K_{sat}$ ) of landslide prone soils is an important parameter for understanding which rainfalls cause instability. However, while many studies have identified a low-conductivity layer to be the cause for shallow landsliding, few studies have attempted to make *in situ* measurements to quantify the contrast between these failure surfaces and the overlying soil mantle, its variability, and the resulting implications on rainfall-rate thresholds. This study utilizes an infiltrometer developed by Nimmo et al. 2009 termed "the bottomless bucket method" to characterize the variability of  $K_{sat}$  in landslide prone materials, specifically on bedrock at the failure plane. This study demonstrates that  $K_{sat}$  is indeed slowest at the plane of failure, and that soil horizon has a strong control on  $K_{sat}$ . Measurements of  $K_{sat}$  and soil mechanical properties provide insight into landslide triggering thresholds for this area, and may be a key component in improving the forecasting of landslide-causing storms.

**Figure 1: A conceptual cross section of a hillslope, portraying conditions that may lead to debris flow initiation. 1A) The advancement of the wetting front. 1B) Buildup of pore fluid pressure on a low-conductivity layer. 1C) Exfiltration of groundwater through bedrock. The dark grey layer at the bottom represents bedrock, and lighter shades represent soils with decreasing shear strength. The red dashed lines refer to potential failure planes. Black arrows are potential flow paths of water, either from the unsaturated zone (top) or groundwater (bottom).**



## **II. Landslide Thresholds: Using Empirical Data, Maps, and Models**

Three different methods have been utilized to assess the probability or susceptibility of failure on hillslopes. These methods are the empirical intensity-duration method, geographical information systems (GIS) mapping, and dynamic modeling. A primary limitation of these methods is that assumptions and simplifications are made for soil and bedrock hydrologic properties, or are solely reliant on landslide causing characteristics and data from past landslide causing storms.

The empirical intensity-duration method uses characteristics of landslide triggering storms to develop a rainfall threshold curve. The threshold curve is created using seasonal antecedent rainfall, along with the minimum intensities and durations of storms that caused at least one failure (Cain, 1980; Wilson and Wiczoreck, 1995). The main limitation of this approach is that it only accounts for conditions that previously caused failures, whereas a wide range of values for antecedent rainfall and storm intensity and duration may combine to produce failures. The empirical intensity-duration approach doesn't provide an understanding of how hydrologic processes interact with a landscape in order to predict the location, timing, and the ways that hazard potential may change with land use and climate change (Iverson, 2000).

Empirical mapping of the spatial distribution of landslides have been used to produce landslide hazard maps. Many approaches have used digital elevation maps (DEMs) and geographical information systems (GIS) to analyze the spatial distribution of previous landslide events and landslide-causing parameters, such as topographic gradient, aspect, land use, bedrock geology, distance from faults, and drainage patterns. These characteristics are

overlay with landslide locations to produce areas to which a degree of landslide hazard is assigned, but does not try and predict the timing of failure (Casadei, et al., 2003)

Mechanistic modeling has been proposed to forecast landsliding. Models generally couple a hydrologic model with an infinite slope model to compute the factor of safety for a given area and time step. Many landslide-prediction models calibrate, approximate, or assume spatial uniformity in soil hydrologic parameters across a hillslope. Early models proposed by Okimura (1989) and Wu and Sidle (1995) routed all rainfall recharge directly to the saturated zone and neglected unsaturated zone storage. More recent models developed by Casadei and Dietrich (2003), (Rosso, et al., 2006), and (Sorbino, 2010) use dynamic shallow subsurface runoff models, but often results in spatial and temporal over prediction of instabilities.

Currently, neither the empirical mapping of the spatial distribution of landslides, the empirical intensity-duration threshold approach, nor mechanistic modeling forecasts the initiation of debris flows with an acceptable level of confidence. These methods and models provide insight on the controls of shallow landslides, but field data and analysis are still required (Rosso, et al., 2006). Particularly, a deep understanding of in situ soil conditions is needed for landslide-prediction models to achieve significant results (Sorbino, 2010).

#### ***A. Previous Work on Debris Flows and $K_{sat}$***

In previous work, the bottomless bucket method has been used to determine infiltration rates of topsoils and failure planes of historic landslide sites in Marin County, California. By making one measurement each of the topsoil and the failure plane per landslide on circa 20 landslides, it was observed that landslides exhibit a low conductivity impedance layer that coincides with failure plane location (Stock et al., in prep). Failure of

the overlying colluvium occurred at the contact of either: low-conductivity colluvium, saprolite, or bedrock. It was found that  $K_{sat}$  values at failure planes ranged from 1-20 mm/hour, with a median value of 8.32 mm/hr, whereas in topsoils they ranged from 11-114 mm/hr, with a median value of 35.6 mm/hr. Furthermore, a tension infiltrometer was implemented on soils in the same location as the bottomless bucket. Results indicate that the two methods produce significantly similar values for  $K_{sat}$  (Stock et al., in prep). This study will build on these observations to provide infiltration data on the variation of  $K_{sat}$  at depth, at the failure plane, and within a single slide area.

### **III. Overview and Objectives**

The objective of this study is to determine the spatial variability of soil hydraulic properties at landslide sites and the resulting impact on the timing and probability of storm-induced landsliding. This goal is achieved by answering critical questions regarding how these landslides fail and what the infiltration rates are in the overlying soils:

- Question 1: Are the landslides at Sedgwick Ranch, Ca caused by the buildup of pore-fluid pressure at the soil-bedrock interface?
- Question 2: How does saturated hydraulic conductivity vary throughout the soil column and at what rates will water pond at the failure plane and subsequently cause failure?
- Question 3: Are there discernable differences in infiltration rates and mechanical properties of soil in varied bedrock and vegetation types that affect slope stability?

These questions were answered by measuring the *in situ* hydraulic and material properties of the soil and bedrock. Furthermore, since all mechanical and hydrologic

variables that affect slope stability have been measured, it allows for an estimation of the timing at which a transient perched water table will form, and therefore, a prediction of the hillslope response to heavy rainfall may be made. This is addressed by utilizing a finite slope model to account for lateral root cohesion developed Gabet and Dunne (2002) to determine slope stability for various perched water table heights.

The scientific opportunity in this work is to explore new data on the hydraulic conductivity of shallow landslide-prone materials as well as the effects of soil and bedrock characteristics on  $K_{sat}$ . Progress in understanding these controls will have a clear practical application on developing new landscape evolution models and how we identify potential landslide causing storms.

#### ***A. Landslide Warning Systems***

Prediction of landslide producing storms is becoming a more realistic goal now more than ever. Over the last decade, the United States Geologic Survey (USGS), in conjunction with The National Weather Service (NWS), have been developing early warning systems for Seattle, Washington, the San Francisco Bay Region, and several counties in Southern California (Chleborad 2003, Wilson and others 1993, Wilson and Wiczorek 1995, NOAA-USGS Debris-Flow Task force, 2005). Warning systems utilize a combination of landslide hazard mapping, modeling, rainfall forecasts, real-time rainfall data, and intensity-duration thresholds based on empirical data from past landslide causing storms. This includes urban and mountainous areas in the city of Seattle, Wa., and the San Francisco Bay Region. However, for southern California, the only existing prototype on debris flow thresholds include areas recently burned by wildfires and the use of real-time rainfall data coupled with an empirical intensity-duration threshold. The potential for the system in southern California

may be greatly improved by refining these thresholds with supplementary data, especially by developing thresholds that are more geographically specific, as well as creating separate thresholds for debris flow and flash floods (NOAA-USGS Debris-Flow Task force, 2005).

### ***B. Landform Evolution and Sediment Delivery***

Landsliding and runoff processes drive erosion and sediment transport.

Understanding the hydrologic factors and thresholds for this redistribution of material has important implications for identifying climate controls on sediment transport and landform evolution (see Dunne, 1991). Rates of sediment delivery from hillslopes may also affect other areas of public concern such as water quality and infilling of debris basins and dams constructed for water storage (Lave and Burbank, 2004). Previous studies in Southern California suggest that landsliding may be responsible for the majority of sediment delivered from small watersheds (Rice and Foggin, 1971).

It is now well known that shallow landslides typically occur in colluvial hollows, also known as zero order basins (see Dietrich and Dunne, 1978 This was the original defining paper on bedrock hollows, but a clearer description and figures can be found in Dunne 1998). These features of the landscape are located in concave bedrock depressions on a hillslope that isn't occupied by channels. Within these swales, or hollows, subsurface flow converges and positive pore-fluid pressures are generated during heavy rainstorms. Upslope colluvium that accumulates in these areas of topographic convergence pose an increased propensity for landsliding. This occurs because their increased soil depths result in a decrease in root strength per unit volume of soil and therefore, a decrease in cohesion. Hollow formation is cyclic: a mass wasting event evacuates colluvium from a hollow and scours the bedrock, further deepening the hollow, the scar heals, filling with colluvium from

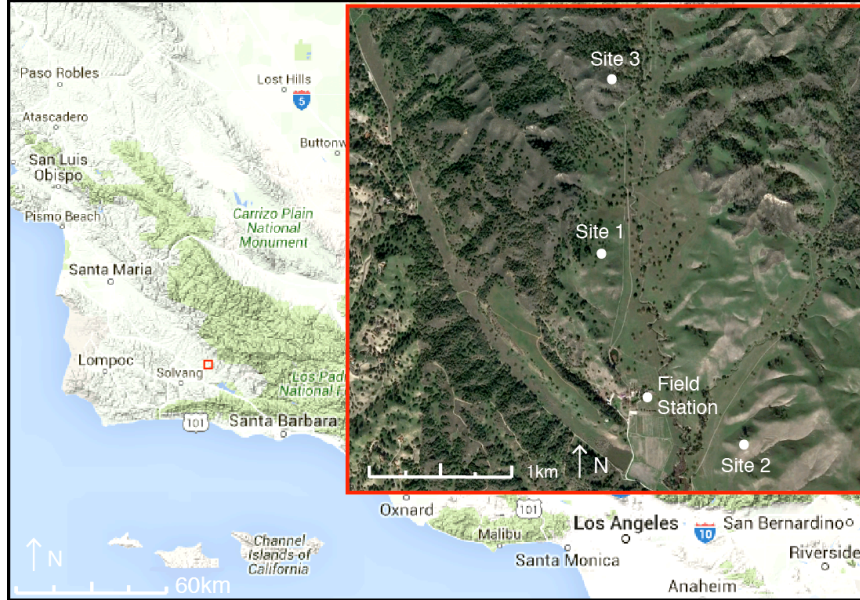
upslope, and finally, it fails again. This process may be repeated a number of times on a variety of timescales, but is generally thought to increase in frequency with time as the hollow grows wider and deeper (Dunne, 1998). In time, 10,000's – 100,000's of years, this cycle will create a synchronous spacing of ridges and “u” or “v” shaped swales within the landscape. The initial stages of this process can be seen at Sedgwick Reserve, where recent changes in the landscape due to uplift and deposition of sediment during the Pleistocene have created planer ridges with insufficient time for the hollow-forming process to deeply fret the planar surfaces.

### ***C. Study Site***

Sedgwick Ranch is part of the University California Natural Reserve System and encompasses 60 km<sup>2</sup> in Santa Barbara County, about 12 km northeast of the town of Los Olivos, CA (Figure 2). The reserve is situated in the northern section of the Santa Ynez Valley, in the western Transverse Ranges, and at the base of the southern slopes of the San Rafael mountains, and is bisected by the Little Pine fault: a north dipping reverse fault that runs northwest-southeast and separates the Pleistocene Paso Robles Formation fanglomerates from Franciscan Formation mélangé to the north (Hall, 1981). The Paso Robles Formation here is described as a weakly consolidated conglomerate composed largely of Monterey shale (Hall, 1981). The overlying soil mantle consists of sandy loams and silty clays which have been observed to contain subrounded-subangular pebble-sized clasts of Monterey shale and Franciscan formation rocks (Gessler et al. 2000). The soils here generally increase in clay content and decrease in organic content with depth (Gessler et al. 2000). The study area consists of a series of gentle to moderately steep rolling hills that have an average relief of 60-100 m. The hills exhibit a series of convex to concave components,

and are separated by channels and streams. Vegetation at the field sites are dominated by either annual Mediterranean grasses, backbrush chaparral, and coastal sage scrub (Gessler et al. 2000).

**Figure 2: Map displaying Santa Barbara County and Sedgwick Reserve, CA. The red square delineates the margins of the field area. Map data: Google Earth, 2016.**



#### ***D. Climate***

The climate in Santa Barbara County is characteristic of the semiarid Mediterranean climate zone and experiences moist mild winters and dry summers. Average annual precipitation is 500 mm/yr with the wettest months occurring from December through March, but is highly variable (County of Santa Barbara Water Resources). Exemplifying this variability, the El Nino of 1997-98' brought 961 mm of rain to Sedgwick Reserve, the wettest year on record (Figure 4).

Weather in southern California strongly is strongly influenced by the North Pacific and California currents of the Pacific Ocean. California usually exhibits a mild climate, but, occasionally it will experience bouts of intense rainfall due to atmospheric rivers: narrow

regions in the atmosphere that transport high vapor content to the midlatitudes. Atmospheric rivers are associated with heavy rain and flooding on the West coast, and have been known to provide 25 to 50% of California's yearly precipitation in just a few events (Ralph et al. 2006) (Figure 3). At present, climate projections typically indicate more extreme atmospheric rivers in the 21<sup>st</sup> century (Detinger et al. 2011). With knowledge of the overall propagation direction of an atmospheric river and information regarding the duration and seasonality factors, it is possible to forecast extreme events, as well as storm-total precipitation (Ralph 2013). Certainly as we expect more extreme rainfall events, and therefore, increased debris-flow activity in the California Coast Ranges, it warrants our time and resources to investigate the controls and timing of debris-flow initiation in order to identify rainfall thresholds that can be used to provide warnings to agencies who can then inform the public.

#### ***E. Precipitation during the 1997-98' El Nino***

The nearest rain gauge to Sedgwick Reserve that recorded the 1997-98' event is located at Figueroa Mountain Station, 4.5 km from the study site. Average rainfall at this station over the last 30 years is 544 mm/yr, and during 1997-98, 1164 mm of rain was recorded (Figure 4). Rainfall at this station is recorded in 24 hour intervals. The largest storm occurred on February, 3, 1998, dropping 104 mm of rain. Unfortunately, intensity-duration data from this particular station are missing for the 1997-1998 events. The nearest rain gauge that recorded rainfall intensities during 1997-98' is located in Foxen Canyon, 9.5 km away from the study area. Average and maximum rainfall intensities at various time intervals for Foxen Canyon correspond with a recurrence interval of 10-25 years for this area.

**Figure 3: Visualization of an atmospheric river over the Pacific Ocean striking the coast of southern California. The scale below represents integrated water vapor (IWV) in  $\text{kg/m}^2$ . IWV is equivalent to total precipitable water content. Figure from NOAA.**

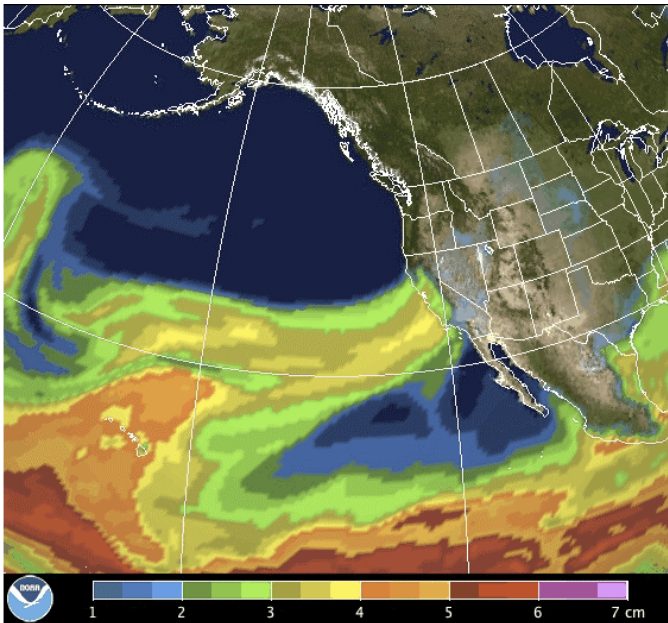
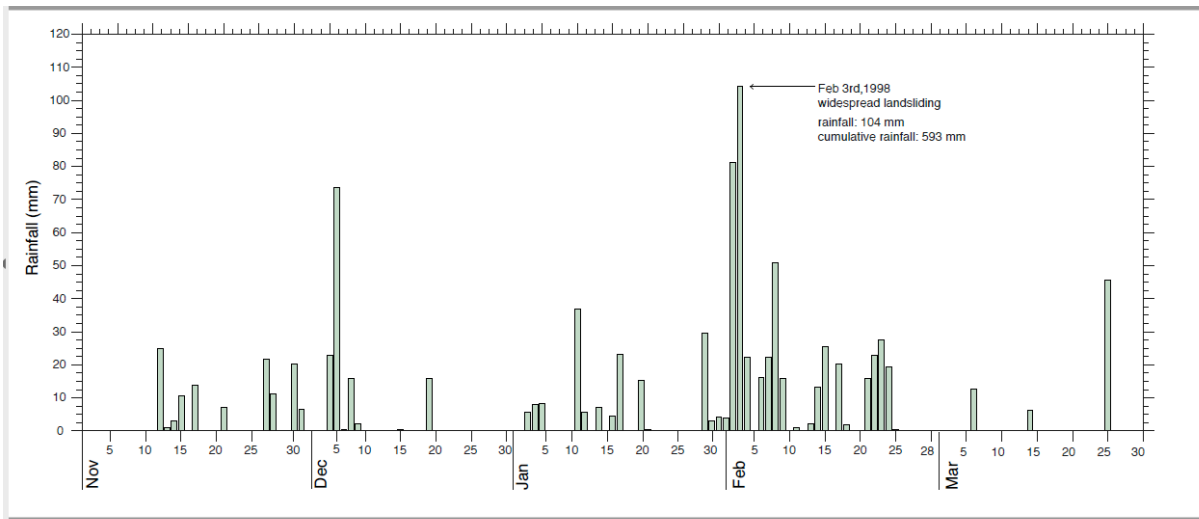


**Figure 4: Daily rainfall totals from the Figueroa Mountain Ranger Station (3 km NE of Sedgwick Reserve). Landsliding occurred on Feb 3<sup>rd</sup>, 1998. Data acquired from NOAA.**



### ***F. Landsliding at Sedgwick Reserve***

During the El Nino of 1997-98, Southern California experienced record rainfalls, and on February 3-4, 1998, more than 150 landslides were triggered during and after several

days of heavy rainfall at Sedgwick Ranch, Santa Barbara County, California. Slope failures occurred as slumps, soil slips, and debris flows in grasslands as well as debris flows in coastal sage (Gabet and Dunne, 2002). In many instances, the initial movement of saturated soil resulted in a reconstitution of the material into a viscous debris flow which travelled down slope until reaching a gradient where deposition occurred, commonly  $<15^\circ$ . The initial failures were slab shaped, with width to length ratios of 1:3 for grasslands and sage (Gabet and Dunne, 2002). Following the scheme of Rice and Foggin (1971) and Campbell (1975), the landslides investigated in this study are best characterized as “soil slips” that reconstituted downslope as “debris flows,” or “silt flows,” a subclass more specific of grain size. Therefore, the landslides investigated in this study are referred to as debris flows.

Slope failures at Sedgwick Reserve that occurred during the 1997-98 El Nino were investigated by Gabet and Dunne (2002) to better understand the role of vegetation conversion on rates and mechanics of shallow landsliding in this area. To do this, they mapped and surveyed circa 30 slope failures to analyze the flux of sediment delivered to valley floors, from both the grasslands and coastal sage. In determining how root reinforcement influences the failure volume and shape of failure, Gabet and Dunne also developed a finite slope model to account for lateral root cohesion, and demonstrated its significant role in slope stability.

Slope stability analyses on debris flows at Sedgwick suggests that there is an inverse relationship between hillslope angle and landslide volume in the sage, however, failure volumes in the grasslands are not slope dependent and are generally smaller. Even though failures in the grasslands occurred at a greater frequency, smaller landslide volumes and

shorter transport distances meant that the coastal sage was most effective in delivering sediment to valley floors over longer time scales (Gabet and Dunne, 2002).

### ***G. Soil-Water Dynamics at Sedgwick***

Throughout the El Nino of 1997-98 and the subsequent La Nina of 1998-99, nine volumetric soil-water depth profiles were monitored using TDR probes along a nearby grass-dominated hillslope at Sedgwick Reserve by Chamran et al. (2002). The results of this study include a characterization of dominant hydrological patterns of soil-water storage and lateral flow redistributions along the hillslope by the use of a one-dimensional water balance model. The paper demonstrates that differences in water storage and availability are highly modified by climatic conditions and local topography, and shows that even a one-dimensional model is suitable for estimating changes in soil-water content on particular hillslopes.

TDR data shows that in early February, 1998 (the timing of landslide triggering at Sedgwick), soil profiles exhibited a sudden increase moisture level by 15-20%, the highest recorded over the two-year period (Chamran et al., 2002). Also, once field capacity had been reached, water was laterally distributed from convex profiles on the hillslope to concave profiles downslope. In other words, after the soil has been sufficiently wetted, soil-water storage became a direct function of topography (i.e., upslope drainage area and slope). During this period, drying of the soil between rainfall events was also shown to be gradual, where dry down was not achieved until June 1998.

## **IV. Methods**

### ***A. Selection of Landslide Sites***

Sedgwick Ranch was chosen as a field site due to its accessibility, abundance of debris flow scars, and available data from previous research (see Gabet and Dunne 2002 and Chamran et al. 2002). Storm induced landslides at Sedgwick Ranch from 1998 were mapped by (Gabet and Dunne 2002) using two sets of aerial photographs at 1:21,000 scale. These sets of aerial photographs include one taken before the landsliding, and another taken after. Landslides were then mapped onto a U.S. Geological Survey Los Olivos 7.5' topographic map. This map was used to locate historic debris flows in the field. Three debris-flow sites were chosen to perform measurements of hydraulic conductivity, collect soil samples, and make lithologic descriptions. These three landslide sites were selected based on their preservation, accessibility, and that the failure planes for the sites have been confirmed as the contact between the soil-bedrock interface. Sites for the study were narrowed down even further by selecting sites that fit the criteria above and exhibited closest to average values for hillslope angle, failure width, and failure depth that were measured on circa 20 debris flows by Gabet and Dunne (2002). For each landslide site, four vertical sections, or "pits", were dug into the lateral scarps and four sites within the landslide scar were chosen for sample collection and measurements. A naming system was used to describe the measurement locations: Site 1-pit 1 corresponds to the first of four pits at site 1, and site 1-FP 1 refers to the first measurement made directly on the failure plane at site 1.

### ***B. Landslide and Soil Morphological Descriptions***

Sites were first classified by their vegetation type, underlying bedrock, hillslope position, and hillslope concavity. Soil profiles at each pit were described using the USDA

(2012) “Field Book for Describing and Sampling Soils.” Soil structure, root density, color, and boundary type was described for each distinct soil horizon. Soil thicknesses of each horizon and depth to failure plane were measured in each pit with a tape. Bedrock was described using USDA (2012).

### ***C. Estimating $K_{sat}$***

The goal of this study was to characterize the variability in hydrologic properties of landslide prone soils by estimating  $K_{sat}$  through the materials of historic landslides. When measuring hydraulic conductivity over broad and remote areas, portability and ease of implementation are important considerations. Therefore, a simplified falling-head single-ring infiltrometer, developed by Nimmo et al. (2009), was utilized to estimate the hydraulic conductivity of soils and bedrock. The method is termed and referred to as the “bottomless bucket method.” This methodology for estimating hydraulic conductivity can be done in 30-40 minutes and is consistent with more rigorous and time-consuming methods of measuring hydraulic conductivity (Nimmo et al., 2009).

Implementation of the procedure includes a vertical-sided bottomless bucket, small shovel, a stopwatch, ruler, and several liters of water (Figure 5). The bucket used in the study is 20 cm high, and has a diameter of 24 cm at the top and bottom. A ruler was attached to the side of the bucket with a clip to measure the amount of infiltrated water.

Tests were performed on a vertical section of the lateral scarp (the area next to the landslide that didn’t fail). A small area atop the scarp was first cleared of vegetation and leveled. Next, a vertical section was cleaned off and soil descriptions were made. A measurement of  $K_{sat}$  was then performed on the exhumed horizontal surface. A soil sample was then taken directly from the same area for grain size analysis and bulk density

measurements. These steps were repeated at 10-20cm intervals along a vertical profile for each distinct soil horizon, at the failure plane, and finally to a depth of at least 20cm below the failure plane (around a meter). Four vertical sections were measured, and four additional measurements were made on the failure plane within a landslide scar, totaling 24 measurements per landslide.

A small area was first cleared of vegetation and leveled to perform measurements. In order to prevent lateral leakage, a small trench approximately 1-3 cm deep was dug with a trowel to place the bottomless bucket into. The bucket was positioned in the trench so that the bottom rim wasn't impeded by loose material. I found that using a small amount of water to first wet the surface, allowed the bucket to be inserted into the ground much more easily. Plumber's putty was then used around the edge of the bucket to create a seal, since the plumber's putty adhered to moistened soil, forming a stronger seal. These steps were performed carefully; making sure the testing area was disturbed as little as possible. Once the bucket edges were sealed, the height of the bucket and the bottom diameter were measured in four locations and averaged for use in the calculation of  $K_{sat}$ . A small piece of plastic was laid in the bucket to minimize surface disturbance. Three to four liters of water was then poured into the bucket, and the plastic was removed. Once the plastic was removed, the stopwatch was started and the initial level of the water recorded. The water level within the bucket was recorded, in mm, in one or two-minute intervals until the surface was exposed after 20-30 minutes of consistent infiltration. It took 20-30 minutes on average to reach a constant infiltration rate. Constant infiltration was rarely achieved during the first test; so consecutive tests were performed. In most cases, a third bucket test was

implemented.  $K_{sat}$  values that are used in the interpretation and plotting of data are calculated from at least 20 min of constant infiltration.

$K_{sat}$  was calculated using Equation 1, as described by Nimmo et al. (2009). This formula uses the dimensions and depth of insertion of the bucket and the capillary length of the soil to mathematically correct for the sorption, positive head, and radial-divergent effects of the wetting front.  $C_1$  and  $C_2$  are empirically determined constants from Reynolds et al. (2002) and are 0.933 and 0.578, respectively. Depth  $d$  and the ring radius  $b$  refer to the depth of ring insertion and the dimensions of the bottomless bucket, respectively. The value of  $\lambda$ , macroscopic capillary length, is a measure of the capillary action of the soil. The effect of  $\lambda$  on  $K_{sat}$  is slight and, therefore, it is appropriate to use a value defined by the textural and structural properties of the soil (Elrick et al., 1989; Nimmo et al., 2009). The macroscopic capillary length used in our calculations is 25 cm, the average value for the soil type, silt loam.  $D_0$  is a measured value for the initial depth of ponding and  $D$  is the measured depth after time  $t$  has elapsed. The formula can be applied whether or not measurements are made until the water has infiltrated completely.

**Equation 1:**

$$K_{sat} = \frac{L_G}{t} \ln \left[ \frac{L_G + \lambda + D_0}{L_G + \lambda + D} \right]$$

The term  $L_G$  is the ring-installation scaling length, and is applied to correct for radial divergence effects below a specific insertion depth:

**Equation 2:**

$$L_G = C_1 d + C_2 b,$$

where  $L_G$  = ring-installation scaling depth;  $t$  = time;  $\lambda$  = macroscopic capillary length of soil;  $D_0$  = initial depth of ponding;  $D$  = depth of ponding;  $d$  = depth;  $b$  = ring radius;  $C_1$  = constant 1 (0.993); and  $C_2$  = constant 2 (0.578).

Measurements of  $K_{sat}$  were made in the winter and spring months, February through April 2015, when moisture was still present in the soil, therefore, avoiding the potential problem of shrinking clays and minimizing the effects of seasonal changes in  $K_{sat}$ . Presumably, this is also the appropriate time when soils are sufficiently wet during the winter/spring landsliding season. Furthermore, it lowered the required amount of water needed to saturate the soils, since one may have underestimated the weight of tens of gallons of water until repeatedly slogging it uphill.

**Figure 5: The falling-head single-ring infiltrometer, or bottomless bucket, used to make  $K_{sat}$  measurements. Plumber's putty was used to seal the outer edges to prevent leakage. A ruler was attached to the side to measure the rate of infiltration.**



#### ***D. Grain size Analysis***

Grain size distributions were measured to determine their effect on infiltration. Samples were taken directly from the area in which infiltration measurements were performed. Samples for grain size were also taken directly above the failure plane to determine if significant differences exist. To measure grain size distributions, a CILAS 1190L particle analyzer was used. A pre-treatment prior to grain size analysis was

performed to remove organic and carbonate content. Procedures from (Kirby et al. 2014) were followed for pre-treatment.  $H_2O_2$  and HCl were used to remove organics and carbonate, respectively. Size fractions for each soil sample were then measured by laser diffraction using the Cilas particle analyzer. The grain size distribution measured by the Cilas particle analyzer includes particles up to 2 mm and finer.

### ***E. Bulk Density***

To determine bulk density, sampling and measurement techniques were performed according to ASTM D 2937-10 “Standard Test for Density of Soil in Place by the Drive Cylinder Method.” Samples were taken from the same column of soil as infiltration measurements. A typical hand-held, hammer-driven core sampler was used to collect a core undisturbed soil. The soil’s mass was then weighed, dried in an oven at 100°C for 12 hours, and then weighed again to calculate the ratio of the mass of dry soil to the volume of the soil sample. If the sample was sandy or loose, the cylinder and soil sample were weighed together and the dimensions of the soil sample were measured in the cylinder.

### ***F. Shear Tests***

Undrained direct-shear tests were performed on undisturbed soil samples. The results of this test were used to determine the shearing properties of soil immediately above the failure plane. The internal angle of friction and cohesion of the soil were estimated based on the results. Samples were collected at the base of the soil column using a hand-held, hammer driven core sampler. Direct shear tests were performed according to ASTM standard D-3080M-11 "Standard Method for Direct Shear Test on Soils under Consolidated Undrained Conditions." For each sample, three separate measurements of shear strength were made

with applied normal forces at 24, 48, and 72 kPa at a constant shear rate. These measurements were then graphically displayed as shear stress vs. normal stress.

To approximate the angle of internal friction ( $\Phi$ ) and cohesion ( $c'$ ), the approximated Mohr-Coulomb failure criteria was plotted as the ordinary least squares (OLS) regression line for the three separate tests (see Equation 3). The OLS method is appropriate because it assumes that  $x$ , or the normal force, is an independent variable that is known with certainty, and that  $y$ , the dependent variable, is what is being predicted.

**Equation 3:**

$$\tau_f = c' + \sigma' \tan \phi,$$

where  $\tau_f$  = shear stress at failure;  $c'$  = cohesion;  $\sigma$  = normal stress; and  $\phi$  = internal angle of friction.

***G. Modeling Conditions for Failure***

A slope stability analysis was performed for each debris flow to back calculate the height of the perched water table that initiated failure. Instead of the infinite-slope model, a finite slope model developed by Gabet and Dunne (2002) was used that accounts for lateral-root reinforcement and failure width.

Whereas the infinite-slope model assumes that the forces on the sides of the failure are negligible, the finite slope model accounts for reinforcement along the side scarps of the failure. The terms in the formula represent forces per unit length of slope, rather than forces per unit area of slope, and therefore assumes that the slide is infinitely long but has a finite width (Gabet and Dunne, 2002). The factor of safety ( $f$ ) was calculated using equation 4:

**Equation 4:**

$$f = \frac{C_s \left( \frac{w + 2z \cos \theta}{\sin \alpha} \right) + C_{rl} \left( \frac{w + 2z_{rd} \cos \theta}{\sin \alpha} \right) + wz(\gamma_s - m\gamma_w) \cos^2 \theta \tan \phi}{wz \gamma_s \cos \theta \sin \theta}$$

Variables used in the calculation of  $f$  (from Equation 3) that were measured in this study include: soil cohesion, internal angle of friction, soil depth, hillslope angle, unit weight of wet soil, rooting depth, and failure width. Values for these variables used in the factor of safety calculation are found in Table 1. The unit weight of saturated soil ( $\gamma_s$ ) was obtained from the calculated dry unit weight ( $\gamma_d$ ) of the soil and the corresponding void ratio ( $e$ ) using equation 5:

**Equation 5:**

$$\gamma_s = \gamma_w \frac{e}{1 + e} + \gamma_d$$

where (for equations 4 and 5),  $f$  = factor of safety;  $C_s$  = soil cohesion (kPa);  $C_{rl}$  = lateral root cohesion (kPa);  $w$  = failure width (m);  $z$  = failure depth (m);  $z_{rd}$  = rooting depth measured vertically (m);  $\gamma_w$  = unit weight of wet soil ( $\text{kN m}^{-3}$ );  $\gamma_s$  = unit weight of water ( $\text{kN m}^{-3}$ );  $m$  = fraction of soil column that is saturated;  $\alpha$  = angle of side scarp ( $^\circ$ );  $\theta$  = hillslope angle ( $^\circ$ );  $\phi$  = angle of internal friction ( $^\circ$ );  $e$  = void ratio; and  $\gamma_d$  = unit weight of dry soil ( $\text{kN m}^{-3}$ ).

Values used for root cohesion were obtained from Terwilliger and Waldron (1990), who measured root cohesion values for the grasslands and sage with direct shear tests. Values for grasslands and sage were found to be 1 kPa and 3 kPa, respectively (Terwilliger and Waldron, 1991). The values for root cohesion have two important caveats: 1) It is assumed that root cohesion doesn't change with depth and 2) the lateral distribution of roots is uniform. However, grass roots at the study sites are fairly uniform, such that taking the heterogeneity into account wouldn't significantly affect the stability analysis. Similarly, the same conclusion may be drawn for sage root cohesion by using an average value for rooting depth.

Using the variables and values as described above, the effects of a change in  $m$  (percentage of soil column saturation) on  $f$  (the factor of safety) was calculated for each landslide site. This was done by calculating  $f$  for increasing  $m$ , performed in steps of 0.1

from 0-100, while holding all other variables constant.  $f$  vs.  $m$  was then plotted to determine where  $f < 1$ , where the driving forces exceed the resisting forces and the hillslope is unstable.

#### ***H. Analysis of Infiltration Data***

Measurements were grouped by distinct soil horizon or location in the stratigraphic profile: (A) A soil horizon, (B) B, Bt, and Bk soil horizons, (FP) failure plane, (C) weathered bedrock, and (R) bedrock. A naming system was used for each site and pit location. The naming system is “site #-pit #”. For example, site 1-1 corresponds to site 1-pit 1.

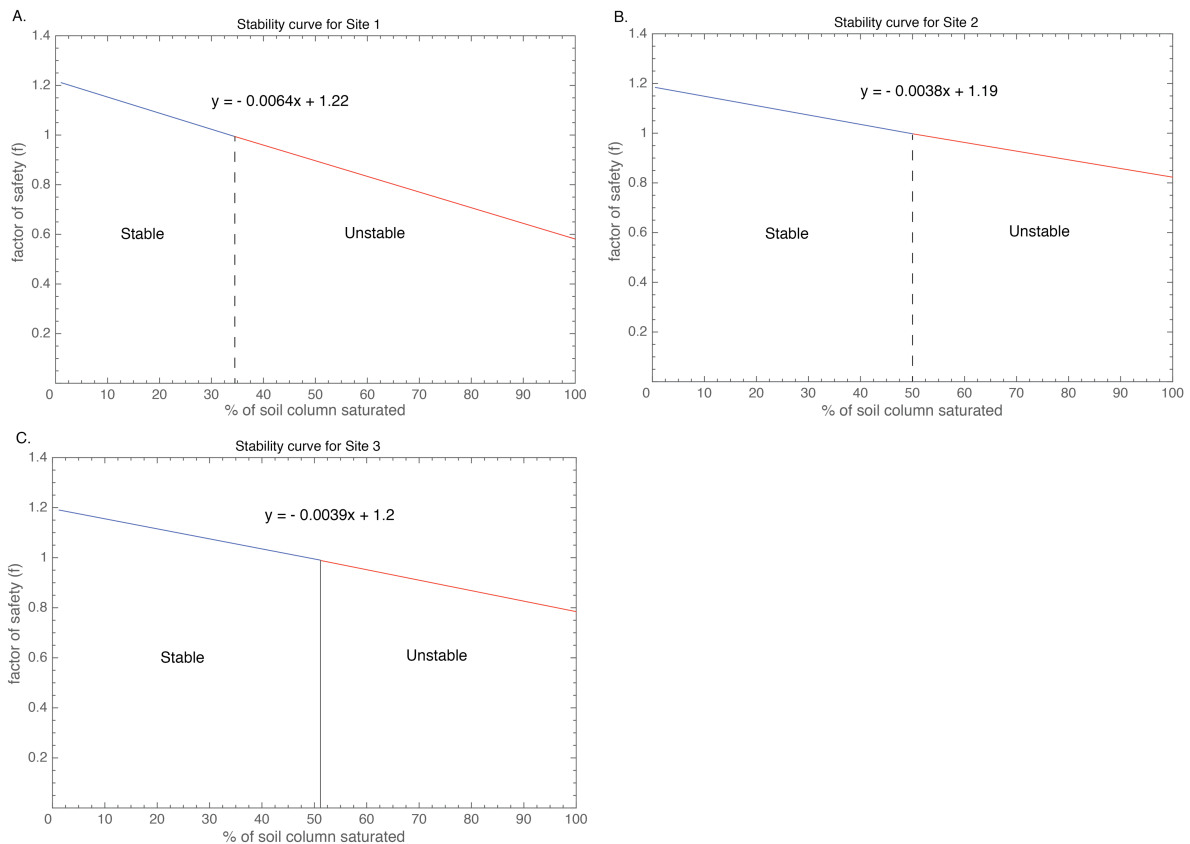
Histograms were created to visualize the distribution and frequency of infiltration measurements. C and R were grouped together in statistical analyses and histograms. A one-sample Kolmogorov-Smirnov (K-S) test was implemented on each dataset to test the null hypothesis, that the sample comes from a population that is normally distributed. Each test was performed at the 95% confidence interval. A two-sample Kolmogorov-Smirnov (K-S) test was implemented to compare the cumulative distributions of the data sets to test the null hypothesis, that both samples are drawn from the same distribution. Each test was performed at the 95% confidence interval.

## V. Results

### A. Stability Analysis

After applying equation 4, each site had certain characteristics in common but each exhibited a unique failure condition. All sites were stable during dry conditions, at  $f > 1$ , and became unstable, at  $f < 1$ , when the soil column was wetted somewhere between 30-50 % of saturation. This is shown graphically for each site in Figure 6. The analysis also indicates that the coastal sage hillslope was most stable when compared to either of the grassland sites. Site 1 failed at 34% of soil column saturation, site 2 failed at 54%, and site 3 failed at 50%.

**Figure 6: A) stability curve for site 1; B) stability curve for site 2; C) stability curve for site 3. At  $m = 0$ , the hillslope is stable, and as  $m$  increases,  $f$  monotonically declines, until  $f < 1$  and failure occurs.**



**B. Site Characterization and Field Observations**

All three sites are characterized as soil slips that failed at the soil-bedrock interface and mobilized as debris flows. Table 1 provides characterization data for the three sites with measurements (scar angle, area, volume, depth, length, width) and descriptive classifications. The soil-landscape pattern at all the sites (which have essentially the same gradient) is generally characterized by a thin, 10–20 cm A horizon, followed by a thicker, 20-90 cm B horizon, or 20-30 cm AC horizon. Soil mantle thicknesses ranged from 30–110 cm with an average thickness of 60 cm. The hillslope position of all three landslide sites is classified as the convex-concave transition. The position of each landslide occurs above the site of channel initiation, where gravity and local slope angle are the dominant processes for sediment transport.

Table 1: Landslide Characteristics

TABLE 1. LANDSLIDE CHARACTERISTICS											
Site	Scar angle	Angle of internal Friction	Cohesion	Vegetation cover	Underlying Bedrock	Hill slope concavity	Area	Volume	Depth	Width	Length
	(°)	(°)	kPa				m <sup>2</sup>	m <sup>3</sup>	m	m	m
SR-1	30	34	0	Grass	Paso Robles Fm.	concave	64	33	0.52	6.9	9.4
SR-2	29	20	9.327	Grass	Monterey Shale	concave	114	84	0.74	5.4	25.6
SR-3	30	22	10.76	Coastal Sage	Paso Robles Fm.	concave	104	94	0.9	8.3	15.6

**C. Site 1**

Failure morphology and locations of measurements for site 1 are shown in Figure 7a. The underlying bedrock at site 1 is Paso Robles formation and the vegetation cover is predominately Mediterranean grasses. Site 1 is situated in a colluvial hollow, where the underlying Paso Robles Fm. forms a “u” shape that begins at the lateral scarps and meets in the center of the slide. This section of the hillslope is an unchanneled portion of the hillslope

that concentrates subsurface flow. The deepest section of the slide is found near the center of the headscarp. As you approach the lateral scarps and the toe of the landslide, soil depth decreases. The soils here are characterized by a thin 10-20 cm A horizon, followed by a 20-35 cm B horizon, and finally, a 8-12 cm Bt horizon (Figure 8a).

The A horizon was subdivided into A<sub>1</sub> and A<sub>2</sub>. A<sub>1</sub> was 11 cm on average and consists of a dark brown gravelly silt loam containing many fine-very fine grass roots and root casts, very friable fine-medium granular peds, and a moderate amount of gopher and worm burrows. A<sub>1</sub> contains vertical cracks that have an average length of 20 cm, 2 mm aperture, and 10 cm spacing that extend to the bottom of A<sub>2</sub>. Few subangular pebbles from the Monterey formation are present. Macropore density decreases with depth. The contact between A<sub>1</sub> and A<sub>2</sub> was gradual.

A<sub>2</sub> was 8 cm on average and consists of a dark brown gravelly silt loam with moderate fine grass roots and root casts, brittle fine-medium granular peds with carbonate coatings, and worm and gopher burrows. A<sub>2</sub> also exhibits prominent vertical cracks extending down from A<sub>1</sub>, and contains a moderate amount of subrounded-subangular, pebble-sized clasts from the Monterey and Franciscan formations. The contact between A<sub>2</sub> and the B horizon was clear.

The B horizon was 12cm on average and consists of a massive, light brown gravelly silt loam with hard-very hard subangular blocky peds. The vertical cracks in the B horizon are similar to A<sub>1</sub> and A<sub>2</sub>, but spaced 15-20 cm apart. The B horizon also contains rounded-subrounded pebble sized clasts from the Monterey and Franciscan formations and very sparse-4mm-tubular roots.

The Bt horizon was only found in pits 1 and 3, was 8 cm on average, and consists of a massive light-reddish brown gravelly silty clay loam with vertical cracks, similar to A<sub>1</sub> and A<sub>2</sub>, but spaced 30-40 cm apart, and contains rounded-subrounded pebble sized clasts of the Monterey and Franciscan formations. The contact between the B horizon and the Paso Robles was sharp.

The Paso Robles Formation at this site was observed as a weakly consolidated clast-supported conglomerate chiefly composed of subrounded-rounded gravel-cobble sized clasts from the Monterey formation. The matrix was found to contain a moderate amount of cemented calcium carbonate at the top of the unit.

#### ***D. Site 2***

Figure 7b displays the morphology of site 2 and the locations of infiltration measurements. The underlying bedrock at this site is the Monterey Formation and the vegetation cover consists predominately of Mediterranean grasses. Similar to site 1, site 2 is also situated in a hollow, where the bedrock was found to be “u” shaped, and converges at the deepest part in the center of the slide. Resistant ridges of Monterey formation flank both sides of the hollow, as seen in figure 7b. Failure occurred near the upper-middle portion of the hillslope at the concave-convex transition. The soil mantle consists of a 20 to 35 cm A horizon, followed by a 10 to 20 cm AC horizon (Figure 8b).

The A horizon consists of a dark brown gravelly silty loam with many fine grass roots and root casts. It contains active gopher and worm burrows and friable-slightly hard fine-medium granular peds. The A horizon contains vertical cracks with an average length of 30 cm, 4 mm aperture, and 10 cm spacing. Some vertical cracks extend from the surface

to the bottom of the AC horizon at the bedrock interface. The contact between the A and AC horizon is gradual.

The AC horizon is similar in composition to the A horizon, except roots and root casts density is decreased. The AC horizon contains a moderate amount of angular pebble sized Monterey Formation clasts.

The underlying bedrock at site 2 was described as very thin-thin bedded Monterey shale that is systematically fractured and moderately weathered. The formation is composed of very fine-grained particles, which are very well sorted. Fresh surfaces are a light-yellowish brown, and the outer surface is white in color. It is moderately soft and tends to break easily into small, 1-5 cm blocky pieces. The range of unconfined compressive strength is 0.60-1.25 Mpa (USDA, 2012). Fractures at the top of the bedrock unit were filled with overlying soil and fine grained particles.

### ***E. Site 3***

Figure 7c displays the morphology of site 3 and the locations of infiltration measurements. Site 3 is located on a concave-convex section of the hillslope. The vegetation cover is coastal sagebrush and chaparral. Failure occurred on the backslope portion of the ridge on a relatively planar section of bedrock. The soil mantle here is thicker than the previous two sites and was measured to be 1.1 m thick at the top of the hillslope, and progressively shallows out to 0.6 m thick as you move away from the headscarp toward the tow of the slide. The soils here are characterized by a thin 5-10 cm A horizon, followed by a 50 to 60 cm B horizon, and lastly, a 20-30 cm Bk horizon (Figure 8c).

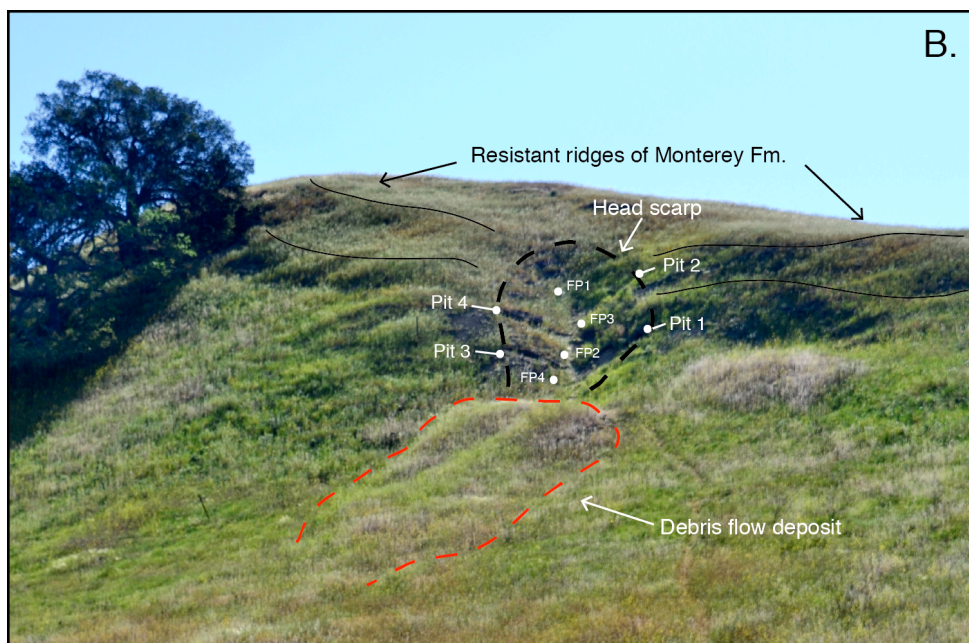
The A horizon was described as a dark brown gravelly silt loam that contains common fine-medium fine roots and root casts as well as few medium sized tubular roots.

The A horizon contains friable slightly hard granular peds and vertical cracks that exhibit a 1-3 mm aperture, 10cm length, and 3 cm spacing on average. The contact between the A and B horizons was found to be clear.

The B horizon consists of a light brown gravelly silt loam with few fine-medium roots and root casts, vertical cracks spaced 10 cm apart, and hard-very hard subangular blocky peds. Carbonate is present, and macropore density decreases with depth. The contact between the B and Bk horizon is clear. The Bk horizon consists of a massive light brown very gravelly silt loam that is relatively high in carbonate content.

The Paso Robles Formation here is described as a weakly consolidated clast-supported conglomerate chiefly composed of subrounded-rounded gravel-cobble sized Monterey formation clasts. The matrix was found to contain a moderate amount of calcium carbonate at the top of the unit.

**Figure 7: Infiltration measurements and pit locations are marked for each site. A dashed black line delineates the head scarp of the debris flow and red dashed lines outline the deposit. A) site 1 B) site 2 C) site 3.**



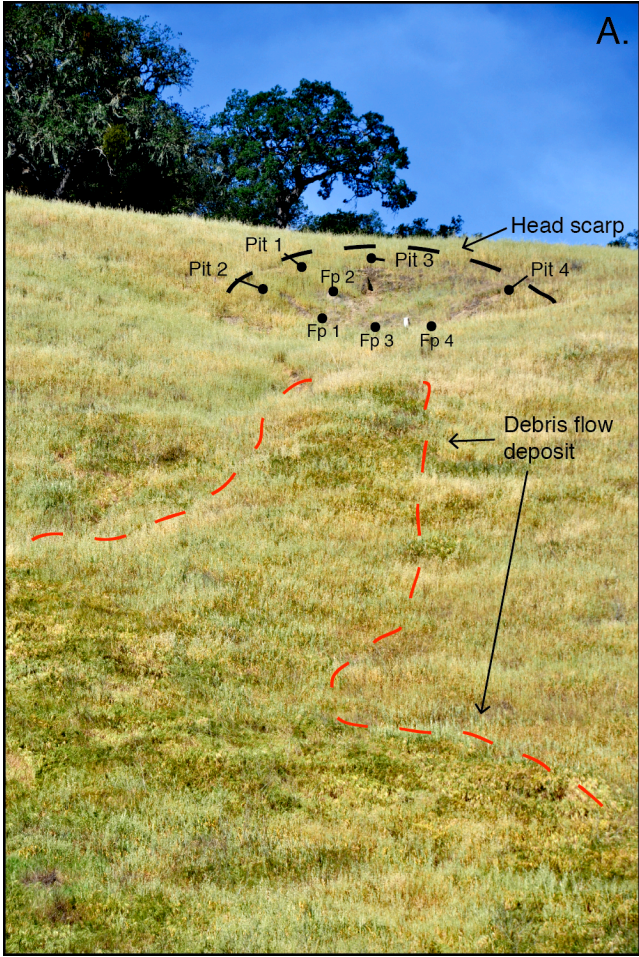
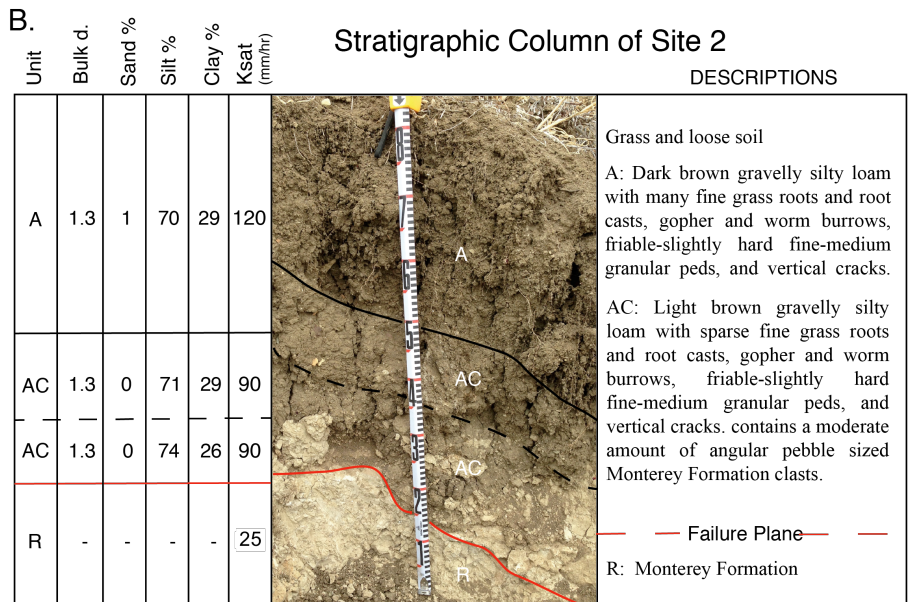
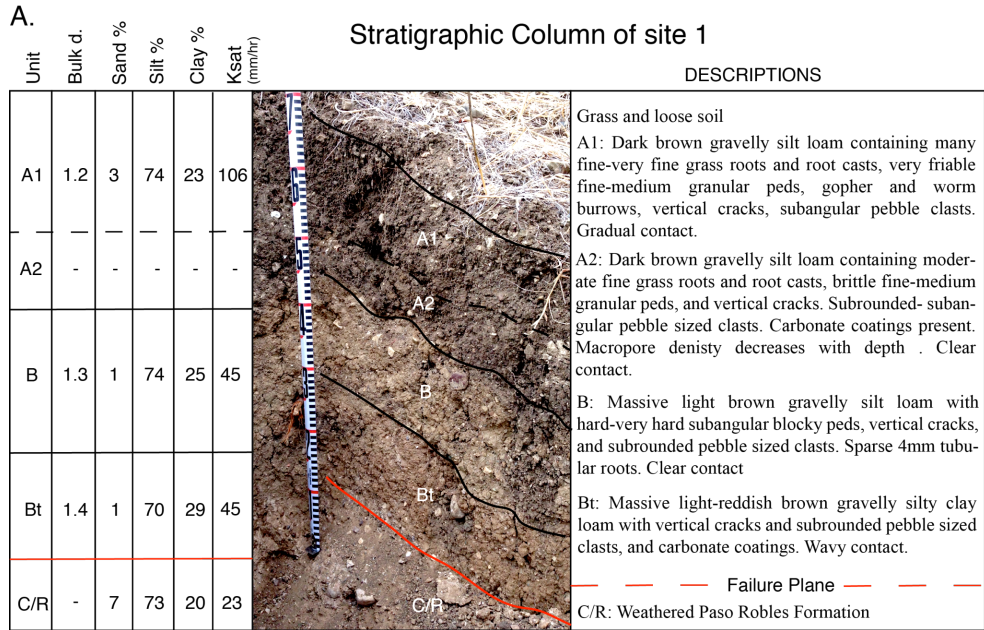
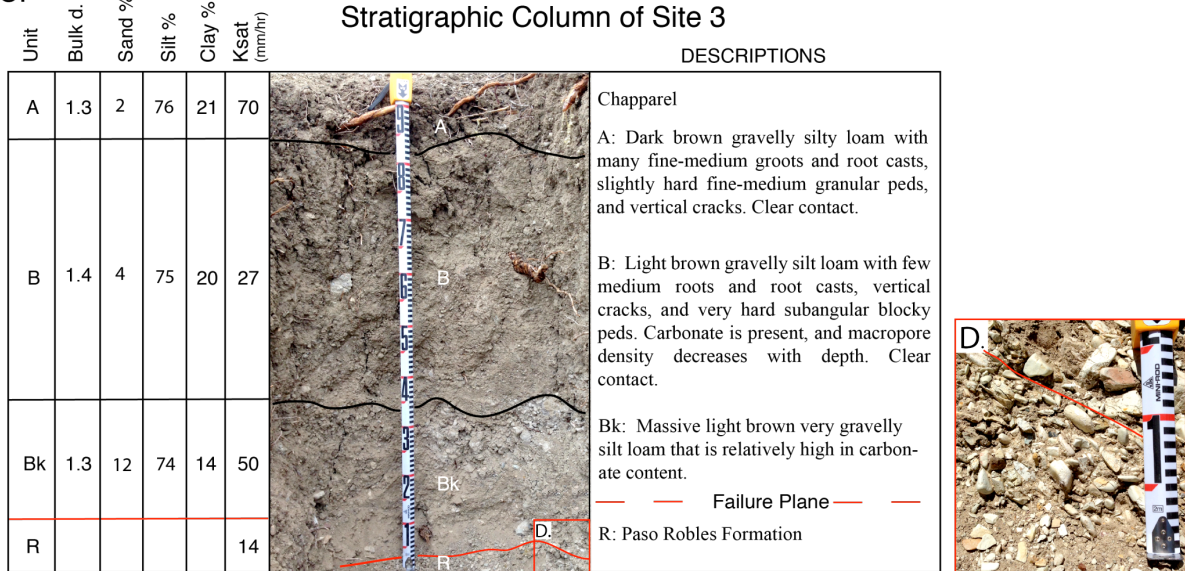


**Figure 8: Stratigraphic columns for sites 1, 2, and 3 with soil descriptions** Average values for particle size and bulk density for all pits and horizons are displayed in columns on the left. The failure plane is marked with a red dashed line. A) Site 1-pit 1. B) Site 2-pit 3 with. Notice at the soil-bedrock contact the weathering of the bedrock, that fractures are filled with overlying soils, and that below the contact, only bedrock exists. Fractures below the soil bedrock interface are open, allowing water to flow freely through them, thus increasing the saturated hydraulic conductivity. C) Site 3-pit 1 D) Paso Robles formation at the failure plane for site 3. Here, the soil-bedrock contact is marked by the infilling of interstitial spaces with overlying fine grained particles and calcium carbonate. Below this contact, small fractures and interstitial spaces are open, and less calcium carbonate exists.



C.

### Stratigraphic Column of Site 3



### F. K<sub>sat</sub> Measurements

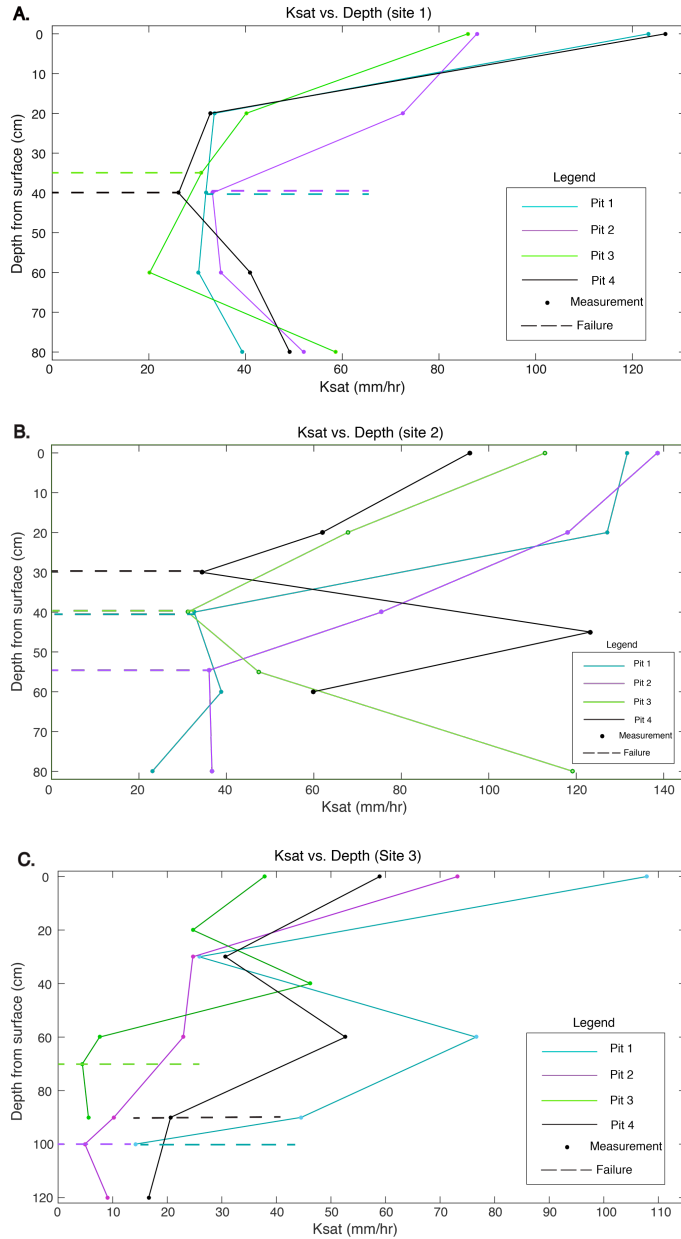
All infiltration, grain size, and bulk density data can be found in the Appendix in tables 3.1-3.3. Table 2.1 provides statistical data for each landslide site and horizon.

Generally, infiltration rates exhibit a similar pattern at all sites. K<sub>sat</sub> is highest at the surface, and then decreases with depth until reaching a minimum at the failure plane (Figure 9).

Below the failure plane, infiltration is variable, either increasing or decreasing, depending on bedrock structure and fracture density. This pattern can be seen clearly in Figure 9a.

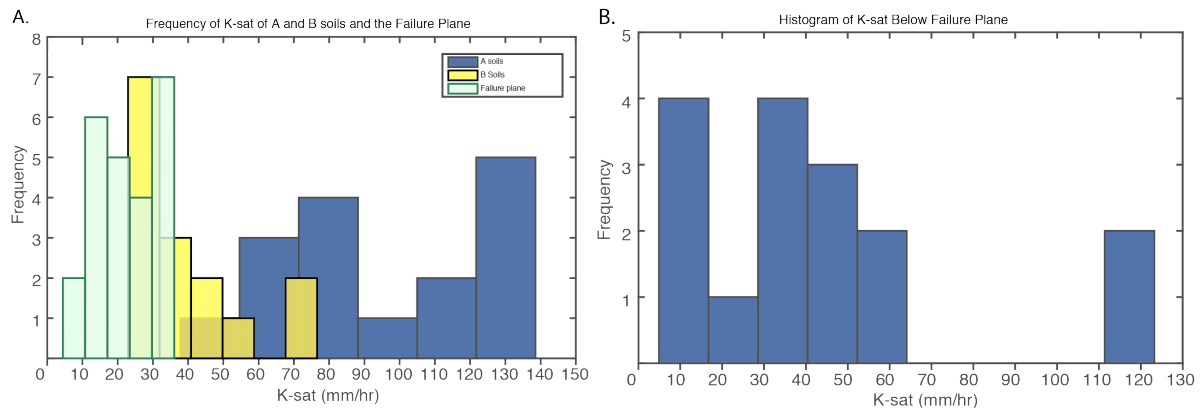
The A horizon exhibits higher values for K<sub>sat</sub> than the B horizon on average. The largest contrast in K<sub>sat</sub> is between the A horizon and the failure plane. Mean K<sub>sat</sub> for the A horizon measurements for all three sites was found to be 94.6 mm/hr ± 7.6 mm/hr, whereas mean K<sub>sat</sub> measurements taken at the failure plane averaged 22.5 mm/hr ± 1.8 mm/hr. K<sub>sat</sub> measurements taken in the B horizons averaged 39.5 mm/hr ± 16.7 mm/hr, and K<sub>sat</sub> measurements taken below the failure plane average 44.4 mm/hr ± 8.7 mm/hr.

**Figure 9: Graph of  $K_{sat}$  vs. depth for sites 1, 2, and 3. A) Graph of  $K_{sat}$  vs. depth for site 1. Notice that all pits exhibit the pattern of fast infiltration at the surface, slowest infiltration at the failure plane, and increased infiltration below the failure plane (fast-slow-fast). The failure plane for each pit is denoted by a dashed line. B) Graph of  $K_{sat}$  vs. depth for site 2. Minimum values of  $K_{sat}$  are observed at the failure plane for 3 out of 4 pits.  $K_{sat}$  at pits 3 and 4 increases rapidly below the failure plane. Infiltration rate variability below the failure plane is attributed to bedrock fracture spacing, density, and amount of infilling from overlying soils. C) Graph of  $K_{sat}$  vs. depth for site 3. Slowest rates of infiltration are found at the failure plane. Notice the convergence and decrease in  $K_{sat}$  at 20-30 cm depth. This is attributed to an increase in clay content, compaction, or calcium carbonate at this horizon.**



Histograms show the relative frequency and distribution of infiltration measurements in each group (Figures 10A and 10B). Soils from the A horizon exhibit the widest distribution, and range from 38-139 mm/hr, whereas  $K_{sat}$  at the failure plane are more tightly distributed and range from 4-33 mm/hr.  $K_{sat}$  values from the A horizon exhibit no overlap with the failure plane.  $K_{sat}$  values in the B horizon range from 25–77 mm/hr. A separate histogram shows the distribution of infiltration rates below the failure plane (figure 8b). With infiltration rates ranging from 5–123 mm/hr, bedrock below the failure plane exhibits a large range of values, overlaps with all other horizons, and contains two peaks centered around 10 and 35 mm/hr. The distribution of  $K_{sat}$  below the failure plane exhibits similar characteristics when compared to the B horizon and Failure plane distributions.

**Figure 10: A) Histograms showing the frequency and distribution of  $K_{sat}$  in the A and B horizons and the failure plane. Note that the failure plane and A horizon measurements do not overlap, and the differences in kurtosis and skewness between the horizons. The failure plane exhibits the most narrow range of values. B) Histogram of  $K_{sat}$  below the failure plane. Note that  $K_{sat}$  exhibits a wide distribution, overlapping with all other horizons and contains two peaks centered around 10 and 35 mm/hr, near the average values for the failure plane and B horizon.**



**G. Kolmogorov-Smirnov tests**

One-sample Kolmogorov-Smirnov (K-S) tests show that none of the individual datasets fit a normal distribution curve. The returned value of H=1 and a P-value of less than .0001 indicates that the null hypothesis can be rejected at  $\alpha= 0.05$  (Table 2.1). Two sample K-S tests on A and B, A and FP, and B and FP show that they are from distinct populations. The returned value of H=1 and P-values  $< .0001$  indicates that the null hypothesis can be rejected at  $\alpha= 0.05$  (Table 2.2).

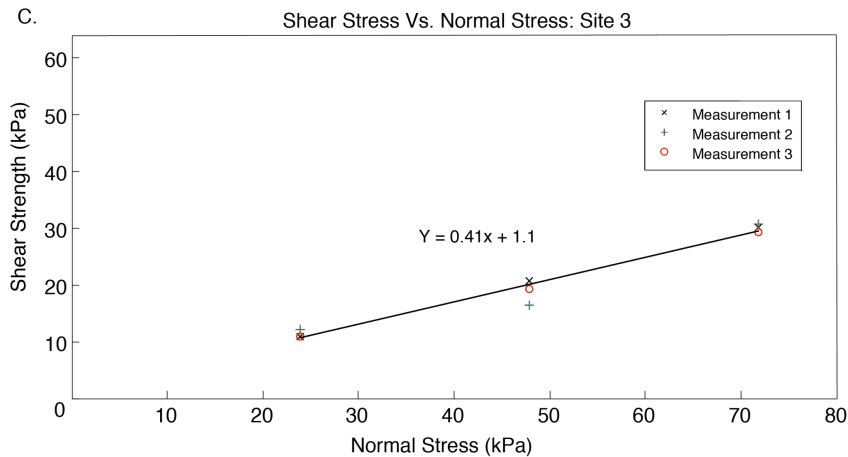
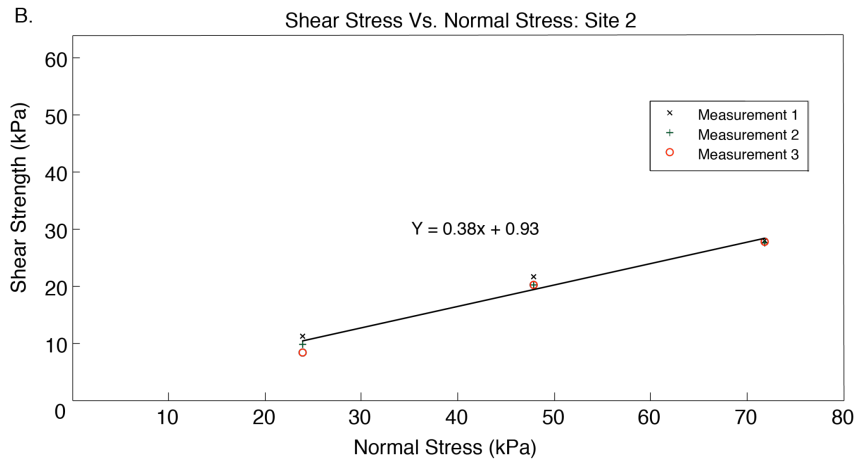
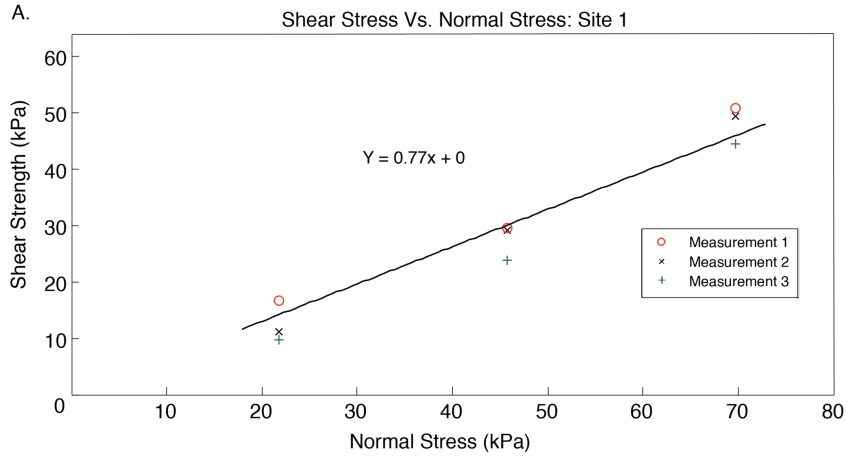
TABLE 2.2 One sample K-S test					TABLE 2.3 Two sample K-S test				
Group	n	H	P	ks stat	Group	n	H	P	ks stat
A	12	1	<0.0001	1	A - B	30	1	0.0027	0.6389
B	18	1	<0.0001	1	A - FP	38	1	<0.0001	1
FP	26	1	<0.0001	1	A - C	31	1	0.0008	0.6795
C	18	1	<0.0001	1	B - FP	36	1	0.0004	0.6111
All	74	1	<0.0001	1	B - C	36	0	0.425	0.2778
*Alpha= 0.05					*Alpha= 0.05				

Tables 2.2 and 2.3

**H. Direct Shear Tests**

The results of the direct shear tests are provided in table 1. Figure 11 shows direct shear measurements with the best fit line and equation for the Mohr Coulomb fracture criteria for each site. Sites SR2 and SR3 both exhibit similar values for cohesion and angle of internal friction. Values for cohesion at SR2 and SR3 were found to be 0.93 and 1.08 kpa and the angle of internal friction was found to be 21° and 22°, respectively. Site 1 was found to be cohesionless and exhibited a higher internal friction angle of 34°. Values of cohesion for sites SR2 and SR3 are comparable to the value of 0.7 Kpa used by Gabet and Dunne (2002).

**Figure 11: A) Direct shear measurements for site 1. B) Direct shear measurements for site 2. C) Direct shear measurements for site 3. The OLS regression lines for the three separate tests are plotted on each graph. The equation of the OLS line that was used to calculate cohesion, and the internal angle of friction is also displayed. Tests were performed at Pacific Soils, Santa Barbara, Ca**



### ***I. Grain Size***

Grain size data show that clay and silt fraction increases with depth. However, this increase is very slight and generally varies by approximately 1-5% (tables 3.1, 3.2, 3.3). In the majority of pits, clay and silt fractions increase from the A to the B horizon. In contrast, no specific pattern is recognized from the B horizon to the failure plane. The clay or silt fraction exhibits an increase at the failure plane in only half of the measured pits, and the increase is not significant.

## **VI. Discussion**

### ***A. Stability Analysis***

The percentage of soil column saturation that was predicted to initiate failure is unique for each failure. This occurs because each site has its own unique set of variables based on measurements from field data e.g., soil cohesion, hillslope angle, internal angle of internal friction, etc. This result is expected, since these parameters are known to be variable in space. This result also highlights the fact that when attempting to predict slope stability over a wide area, the spatial variability of soil hydraulic and mechanical properties should be expected to yield a distribution of threshold m-values. Debris flow sites chosen for this study reflect near-average debris flow size and depth at Sedgwick Reserve. Sufficient measurements of  $K_{sat}$ , particle size, and bulk density have been made to define usable average values for the local area and potentially over a larger regional area with similar soil and bedrock characteristics. However, it remains to be seen if an average value for these parameters may be used to predict an acceptable percentage of failures over a regional area.

The safety factor during dry conditions is close to 1.2 for all three sites and failure is predicted to occur when 30-50% of the soil column above the failure plane is saturated. A

safety factor is 1.2 is generally classified as conditionally stable, and may be an indicator that the factor of safety analysis is an underestimate of hillslope stability during dry conditions. This type of error would increase the percentage of soil column saturation necessary for failure. However, measurements of soil moisture with time-domain reflectometers (TDR) probes were carried out by Chamran et al. (2002) over a 2 ha, zero-order, grass dominated hillslope <1km away from sites 1 and 3. Soil moisture measurements were conducted for 2 years, from 1997-1999, and encapsulate the February 3<sup>rd</sup> storm. The TDR measurements for February 3<sup>rd</sup> show that soil moisture profiles at the top convex portion of the hillslope, where the gradient was low, reached full saturation, whereas downslope profiles in concavities at the concave-convex transition reached levels up to 40% (Chamran et al. 2002). Both profiles also changed drastically, where a change of 10-20% to 30-40% saturation occurred due to the February 3<sup>rd</sup> storm (Chamran et al. 2002). Using measured soil moisture values at the concave-convex transition from Chamran et al. (2002) as an analog for soil moisture conditions at the sites in this study, values of 30-50% of soil saturation during the storm that initiated all debris flows seem reasonable, and such values are predicted to trigger failures based on the stability analysis. An analysis of rainfall and application of a hydrologic model may provide more insight into the timing and level of soil saturation reached at each debris flow site during the 97-98 winter.

The coastal sage hillslope was more stable than either of the grass covered hillslopes. This result is in agreement with the conclusion reached by Gabet and Dunne (2002), where their results show that the grasslands exhibited a greater frequency of failures when compared to the coastal sage for this event. It is expected that this trend will likely be the case for future events. Presumably, this occurs because the coastal sage was cleared and

converted to Mediterranean grasses for ranching purposes decades earlier. The grasses have lower root cohesion than the sage. Therefore, a disequilibrium exists between soil depth and the ability of the grass roots to reinforce the soil, so over time, the soil in the grasslands will attain a shallower equilibrium depth by increasing the frequency of mass wasting events (Gabet and Dunne 2002).

### ***B. Infiltration Measurements and Implications for Hillslope Stability***

By comparing  $K_{sat}$  of the overlying soil horizons to the failure planes, all available evidence indicates that a low-conductivity layer occurs at the failure plane and that  $K_{sat}$  exhibits a strong dependence on soil horizon. This suggests that in order to predict rainfall rate thresholds and the timing of landsliding, soil horizons and their thicknesses must be taken into account, rather than assuming a uniform  $K_{sat}$  for the entire soil column.  $K_{sat}$  data at the failure plane suggest that once the soil reaches field capacity, rainfall exceeding 4-33 mm/hr will facilitate the formation of a temporary perched water table at the soil-bedrock interface, and that rainfall will need to be sustained at these rates in order to trigger shallow landslides in this area.

While each site displays a unique threshold based on hillslope morphology, soil mechanical properties, and vegetation cover, the timing and rainfall thresholds for landsliding may be similar. For example, if you compare the drainage rate of the failure plane to the % saturation above the failure plane predicted to initiate failure, the drainage rate and the % saturation may be such that their thresholds for failure are reached almost synchronously. The drainage rate for site 1 is 27 mm/hr and failure was predicted to occur at 34% of soil saturation. The drainage rate ( $K_{sat}$ ) for site 2 and 3 are 25 and 14 mm/hr and failure is predicted to occur at 50% and 54%, respectively. Even though the % soil saturation

is higher for sites 2 and 3, the drainage rate is slower, allowing for the buildup of a temporary perched water table to occur in a shorter time frame. There are slight discrepancies in soil depth for sites 2 and 3, such that 54% of the soil column for site 2 corresponds to a 0.4 m, and 50% of the soil column for site 3 corresponds to 0.45 m. However, when taking  $K_{sat}$  in the overlying soils and hillslope morphology into account, these discrepancies may even out. This observation and hypothesis suggests that the thresholds for shallow landsliding are dictated not only by hillslope morphology and mechanical properties of the overlying soil mantle, but may be primarily controlled by the hydraulic properties of the soil mantle and discontinuity surfaces. The rate at which landslide prone materials pass water may prove to be a better predictive tool for determining potential landslide causing storms. This hypothesis may be tested with data collected from this study, and the application a hydrologic model for unsaturated zone flow.

### ***C. Failure Plane Formation***

On average,  $K_{sat}$  of surface soils passed water at rates 5 times faster than rates at the failure plane. Similarly, a surprising result is that  $K_{sat}$  is, on average, faster below the failure plane than directly at the failure plane. This pattern of fast-slow-fast infiltration suggests that there is a process that facilitates the formation of the failure plane at the soil bedrock interface or another low conductivity layer.

The first question that arises when considering the infiltration data is: why is there a significant drop in infiltration rate at the failure plane? To answer this question, a number of factors must be considered, such as: grain size distribution, compaction, structure, and organic content.

Previous research shows that organic content declines with depth in soil profiles at Sedgwick Ranch (Gessler et al. 2000). Based on this relationship and field observations, organic content does not play a significant role in the decline of  $K_{sat}$  at the failure plane in these profiles.

The first hypothesis that was developed for the  $K_{sat}$  minimum is related to sediment transport and the grain-size distribution. It was hypothesized that illuviation, or water assisted transport of grains (colloids), may have caused an accumulation of fine grained particles at the base of the soil column (i.e., failure plane), and therefore would result in a reduction of  $K_{sat}$ . However, the grain size data fail to support this hypothesis given that about 50% of the pits exhibit a nominal reduction in grain size at the failure plane.

Given the previous result, a second hypothesis was formed that the reduction in  $K_{sat}$  may be most related to increased compaction and consolidation at the base of the soil column. Since bulk density of soil is an indicator of compaction, bulk density was measured down through the soil column to test this hypothesis.

The data in table 3.1 shows that bulk density increases with depth in 3 out of 4 pits at site 1 until reaching a maximum at the failure plane. Bulk density at site 2 fluctuates only slightly, and the highest values are seen in both the middle and at the base of the soil column. At site 3, the highest values for bulk density are actually found at the surface, correlating to the highest clay content. No other analysis was performed to test whether the increase in bulk density that is observed is sufficient to account for the reduction in  $K_{sat}$  in these locations. However, it is clear that bulk density does not have a strong control on  $K_{sat}$  at the failure plane.

A third explanation for the observed low-conductivity may be related to fine grained particles and calcium carbonate filling in fractures and void spaces within the bedrock at the failure plane, thus decreasing the amount of pathways and linkages for water to flow. For example,  $K_{sat}$  of bedrock, which has fractures that are filled with fine-grained sediment and calcium carbonate would most likely be much lower than when compared to bedrock where both are absent. This is analogous to what is seen in the field. At the soil bedrock interface, bedrock fractures are filled with compacted fine-grained sediment that contains an abundance of calcium carbonate, whereas below the failure plane, bedrock fractures are open and exhibit much less calcium carbonate build up. Thus far, the conclusion is drawn that a combination of these processes: (1) increased compaction, (2) grain size reduction, and (3) infilled bedrock fractures exhibiting calcium carbonate build-up are the causes of a reduction in infiltration at the failure plane, where situation (3) carries the most influence.

It is hypothesized that dynamic processes such as gravitational settling, cementation, and bioturbation all influence  $K_{sat}$  during the evolution of colluvial hollows. Settling and cementation increases with depth and time, causing a decrease  $K_{sat}$ , whereas bioturbation increases  $K_{sat}$ , but decreases with depth. After enough time, compaction from settling and cementation lower  $K_{sat}$  enough that at stochastic intervals, heavy rainfall strips off the material above the failure plane, thus resetting the process of soil accumulation above the failure plane.

#### ***D. Failure Sites and Recurrence Intervals***

It is interpreted that site 1 and site 2 are located in hollows, where the bedrock here has been lowered by higher rates of bedrock weathering, more frequent failure, and incision from past mass wasting events. It is unknown whether these are primary failures, however,

the u shaped profiles of the bedrock in these locations suggest that these are recurring sites for landsliding. These sites may have failed multiple times in the past as they continue the cycle of sediment deposition and evacuation over times scales of 100-1000's of years (Reneau, 1990). The sites are currently undergoing deposition of colluvium, and will eventually heal, masking any evidence of their existence.

In comparison to sites 1 and 2, the bedrock geometry at site 3 has a less pronounced "u" shape, and the hillslope has a more planar shape, suggesting failures at this location initiated later and/or have occurred less frequently. However, the soil depth here is deeper than both sites 1 and 2. This is either a function of the differences in hillslope location or the difference in vegetation cover (coastal sage as opposed to grasslands). Soils in the chaparral may exhibit deeper profiles based on their greater rooting depth and cohesion compared to the grasslands.

Another observational difference between sites located in the grasslands and the coastal sage is the amount of deposition that has occurred within the debris flow scar. Sites 1 and 2 were observed to contain larger amounts of colluvium deposited after the debris flow. The lateral scarps of sites 1 and 2 are also more degraded than site 3. Based on field observations of other debris flow scars in both the coastal sage and grasslands at Sedgwick Reserve, it is hypothesized that healing times and recurrence intervals for debris flows of varying vegetation are significantly different, where debris flows in the grasses heal quicker and failures reoccur more frequently than coastal sage covered hillslopes.

## VII. Conclusions

1. Landslides at Sedgwick Ranch, California failed from the buildup of pore fluid pressure at the soil-bedrock interface.
2.  $K_{\text{sat}}$  has a strong dependence on soil horizon. Distributions of  $K_{\text{sat}}$  in the A and B horizons and at the failure plane are from distinct populations.
3. The distribution of  $K_{\text{sat}}$  at the failure plane exhibits a much smaller standard deviation in comparison to the A and B horizons.
4.  $K_{\text{sat}}$  values at the failure plane ranged from 4 to 33 mm/hr and suggest that rainfall exceeding these rates need to be sustained for several hours to initiate debris flow activity.
5. Causes for the formation of the failure plane are inconclusive, however, field observations suggest that the infilling of fractures with fine-grained particles at the soil-bedrock interface may be the cause of the low-conductivity layer.
6. Rainfall-rate thresholds for shallow landsliding are dictated not only by hillslope morphology and mechanical properties of the overlying soil mantle, but may be primarily controlled by the hydraulic properties of the soil mantle and discontinuity surfaces.

## VII. References

1. Baum, R. L., and Godt, J. W., 2010, Early warning of rainfall-induced shallow landslides and debris flows in the USA: *Landslides*, v. 7, no. 3, p. 259-272.
2. Baum, R. L., Godt, J. W., and Savage, W. Z., 2010, Estimating the timing and location of shallow rainfall-induced landslides using a model for transient, unsaturated infiltration: *Journal of Geophysical Research: Earth Surface* (2003–2012), v. 115, no. F3.
3. Brooks, R. H., and Corey, A. T., 1964, Hydraulic properties of porous media and their relation to drainage design: *Transactions of the ASAE*, v. 7, no. 1, p. 26-0028.
4. Caine, N., 1980, The rainfall intensity: duration control of shallow landslides and debris flows: *Geografiska Annaler. Series A. Physical Geography*, p. 23-27.
5. Campbell, R. H., 1975, *Soil slips, debris flows, and rainstorms in the Santa Monica Mountains and vicinity, southern California*. U.S. Geological Survey Professional paper 851, 50 p.
6. Casadei, M., Dietrich, W., and Miller, N., 2003, Testing a model for predicting the timing and location of shallow landslide initiation in soil-mantled landscapes: *Earth Surface Processes and Landforms*, v. 28, no. 9, p. 925-950.
7. Chamran, F., Gessler, P., and Chadwick, O., 2002, Spatially explicit treatment of soil-water dynamics along a semiarid catena: *Soil Science Society of America Journal*, v. 66, no. 5, p. 1571-1583.
8. Chleborad, A. F., 2003, *Preliminary evaluation of a precipitation threshold for anticipating the occurrence of landslides in the Seattle, Washington, Area*, 2331-1258.
9. Crozier, M., and Preston, N., 1999, *Modelling changes in terrain resistance as a component of landform evolution in unstable hill country*, *Process modelling and landform evolution*, Springer, p. 267-284.
10. Dettinger, M., 2011, Climate change, atmospheric rivers, and floods in California—a multimodel analysis of storm frequency and magnitude changes: *Journal of the American Water Resources Association*, v. 47, p. 514-523.
11. Dietrich, W., and Dunne, T., 1978, Sediment budget for a small catchment in a mountainous terrain.
12. Duan, J., 1996, *A coupled hydrologic-geomorphic model for evaluating effects of vegetation change on watersheds* [Ph.D. Thesis]: Oregon State University. P. 154
13. Dunne, T., Zhang, W., and Aubry, B. F., 1991, Effects of rainfall, vegetation, and microtopography on infiltration and runoff: *Water Resources Research*, v. 27, no. 9, p. 2271-2285.

14. Dunne, T., 1998, *Critical data requirements for prediction of erosion and sedimentation in mountain drainage basins*, Wiley Online Library.
15. Ellen, S.D., and Wieczorek G.F., 1988, *Landslides, Floods, and Marine effects of the storm of Jan 3-5, 1982, in the San Francisco Bay Region, California*: U.S. Geological Survey Professional Paper 1434: U.S. Geological Survey, Denver, CO, 310 p.
16. Force, N.U. D. F. T., 2005, *NOAA-USGS debris-flow warning system: Final Report*, 2330-5703.
17. Gabet, E. J., and Dunne, T., 2002a, Landslides on coastal sage-scrub and grassland hillslopes in a severe El Nino winter: The effects of vegetation conversion on sediment delivery: *Geological Society of America Bulletin*, v. 114, no. 8, p. 983-990.
18. Godt, J., and McKenna, J., 2008, Hydrological response of hillside materials to infiltration: implications for shallow landsliding in the Seattle area: Landslides and engineering geology of the Seattle, Washington, area: *Reviews in Engineering Geology*, v. 20, p. 121-135.
19. Hall, A., Clarence Jr, 1981, *Map of Geology Along the Little Pine Fault, Parts of the Sisquoc, Foxen Canyon, Zaca Lake, Bald Mountain, Los Olivos, Figueroa Mountain Quadrangles, Santa Barbara County, California*: U.S. Geological Survey Miscellaneous Field Studies Map MF-1285, scale 1:24,000
20. Iverson, R. M., 2000, Landslide triggering by rain infiltration: *Water Resources Research*, v. 36, no. 7, p. 1897-1910.
21. Jayko, A., and Blake Jr, M., 1984, Sedimentary petrology of graywacke of the Franciscan Complex in the northern San Francisco Bay Area, California: *Pacific section S.E.P.M.*, v. 43, p. 121-134.
22. Kirby, M. E., Feakins, S. J., Hiner, C. A., Fantozzi, J., Zimmerman, S. R., Dingemans, T., and Mensing, S. A., 2014, Tropical Pacific forcing of Late-Holocene hydrologic variability in the coastal southwest United States: *Quaternary Science Reviews*, v. 102, p. 27-38.
23. Lavé, J., and Burbank, D., 2004, Denudation processes and rates in the Transverse Ranges, southern California: Erosional response of a transitional landscape to external and anthropogenic forcing: *Journal of Geophysical Research: Earth Surface*, v. 109, no. F1.
24. Larsen, I. J., Montgomery, D. R., and Korup, O., 2010, Landslide erosion controlled by hillslope material: *Nature Geoscience*, v. 3, no. 4, p. 247-251.
25. Matsushi, Y., Hattanji, T., and Matsukura, Y., 2006, Mechanisms of shallow landslides on soil-mantled hillslopes with permeable and impermeable bedrocks in the Boso Peninsula, Japan: *Geomorphology*, v. 76, no. 1, p. 92-108.

26. Montgomery, D. R., and Dietrich, W. E., 1994, A physically based model for the topographic control on shallow landsliding: *Water Resources Research*, v. 30, no. 4, p. 1153-1171.
27. Montgomery, D. R., Dietrich, W. E., and Heffner, J. T., 2002, Piezometric response in shallow bedrock at CB1: Implications for runoff generation and landsliding: *Water Resources Research*, v. 38, no. 12, p. 10-11-10-18.
28. Montgomery, D. R., Schmidt, K. M., Dietrich, W. E., and McKean, J., 2009, Instrumental record of debris flow initiation during natural rainfall: Implications for modelling slope stability: *Journal of Geophysical Research: Earth Surface* (2003–2012), v. 114, no. F1.
29. Nimmo, J. R., Schmidt, K. M., Perkins, K. S., and Stock, J. D., 2009, Rapid measurement of field-saturated hydraulic conductivity for areal characterization: *Vadose Zone Journal*, v. 8, no. 1, p. 142-149.
30. Okimura, T., 1989, Prediction of slope failure using the estimated depth of the potential failure layer: *Journal of Natural Disaster Science*, v. 11, no. 1, p. 67-79.
31. Pradel, D., and Raad, G., 1993, Effect of permeability on surficial stability of homogeneous slopes: *Journal of Geotechnical Engineering*, v. 119, no. 2, p. 315-332.
32. Ralph, F., Coleman, T., Neiman, P., Zamora, R., and Dettinger, M., 2013, Observed impacts of duration and seasonality of atmospheric-river landfalls on soil moisture and runoff in coastal northern California: *Journal of Hydrometeorology*, v. 14, no. 2, p. 443-459.
33. Ralph, F. M., Neiman, P. J., Wick, G. A., Gutman, S. I., Dettinger, M. D., Cayan, D. R., and White, A. B., 2006, Flooding on California's Russian River: Role of atmospheric rivers: *Geophysical Research Letters*, v. 33, no. 13.
34. Reneau, S. L., and Dietrich, W. E., 1987, The importance of hollows in debris flow studies; examples from Marin County, California: *Reviews in Engineering Geology*, v. 7, p. 165-180.
35. Reneau, S. L., Dietrich, W. E., Donahue, D. J., JULL, A. T., and Rubin, M., 1990, Late Quaternary history of colluvial deposition and erosion in hollows, central California Coast Ranges: *Geological Society of America Bulletin*, v. 102, no. 7, p. 969-982.
36. Rice, R. M., and Foggin, G., 1971, Effect High Intensity Storms on Soil Slippage on Mountainous Watersheds in Southern California: *Water Resources Research*, v. 7, no. 6, p. 1485-1496.
37. Rosso, R., Rulli, M. C., and Vannucchi, G., 2006, A physically based model for the hydrologic control on shallow landsliding: *Water Resources Research*, v. 42, no. 6.

38. Sidle, R., and Swanston, D., 1982, Analysis of a small debris slide in coastal Alaska: *Canadian Geotechnical Journal*, v. 19, no. 2, p. 167-174.
39. Sorbino, G., Sica, C., and Cascini, L., 2010, Susceptibility analysis of shallow landslides source areas using physically based models: *Natural Hazards*, v. 53, no. 2, p. 313-332.
40. Terlien, M.J., Asch, T.J., Van Westen, C.J., 1995, Deterministic modelling in GIS-based landslide hazard assessment: *Geographical Information System in Assessing Natural Hazard Advances in Natural and Technological Hazards Research*, v 5, p. 57-77
41. Terwilliger, V. J., and Waldron, L. J., 1991, Effects of root reinforcement on soil-slip patterns in the Transverse Ranges of southern California: *Geological Society of America Bulletin*, v. 103, no. 6, p. 775-785.
42. USDA, 2012, Part 631 Geology, National Engineering Handbook: *Chapter 4, Engineering Classification of Rock Materials*. 210-VI-NEH, Amend. 55.
43. Van Asch, T. W., Buma, J., and Van Beek, L., 1999, A view on some hydrological triggering systems in landslides: *Geomorphology*, v. 30, no. 1, p. 25-32.
44. Wilson, R. C., Mark, R. K., and Barbato, G., 1993, Operation of a real-time warning system for debris flows in the San Francisco Bay area, California: *Proceedings, Hydraulic Engineering* (1993), ASCE, p. 1908-1913.
45. Wilson, R.C., and Wieczorek, G.F., 1995, Rainfall thresholds for the initiation of debris flows at La Honda, California: *Environmental and Engineering Geoscience*, v. 1, p. 11-27
46. Wu, W., and Sidle, R. C., 1995, A distributed slope stability model for steep forested basins: *Water Resources Research*, v. 31, no. 8, p. 2097-2110.

## VIII. Appendix

TABLE 3.1 SOIL and BEDROCK CHARACTERISTICS for SITE 1

Pit	Depth cm	Horizon	Ksat mm/hr	Clay %	Silt %	Sand %	Bulk
							density g/cm <sup>3</sup>
1	0	A	123	22.7	71.3	6.1	1.27
1	20	Bt	34	26.1	72.1	1.8	1.30
1	35	FP	32	31.0	68.7	0.3	1.33
1	60	R	30	15.5	71.2	13.4	-
1	80	R	39	-	-	-	-
2	0	A	88	23.7	72.2	4.1	1.15
2	20	Bt	73	27.2	71.7	1.1	1.29
2	40	FP	33	26.1	71.7	2.2	1.39
2	60	R	35	14.6	73.3	12.1	-
2	80	R	52	-	-	-	-
3	0	A	86	19.5	80.2	0.4	1.30
3	20	B	40	20.9	78.2	0.9	1.33
3	35	FP	31	26.3	71.8	1.9	1.47
3	60	R	20	16.6	73.8	9.6	-
3	80	R	59	-	-	-	-
4	0	A	127	24.7	72.5	2.8	1.19
4	20	B	33	26.7	73.0	0.3	1.31
4	40	FP	26	25.0	73.9	1.0	1.45
4	60	R	41	21.8	76.7	1.5	-
4	80	R	49	-	-	-	-
FP	FP-1	FP	18	-	-	-	-
FP	FP-2	FP	26	-	-	-	-
FP	FP-3	FP	25	-	-	-	-
FP	FP-4	FP	27	-	-	-	-

TABLE 3.2 SOIL and BEDROCK CHARACTERISTICS for SITE 2

Pit	Depth cm	Horizon	Ksat mm/hr	Clay %	Silt %	Sand %	Bulk
							density g/cm <sup>3</sup>
1	0	A	132	24.3	73.4	2.3	1.20
1	20	AC	127	25.9	73.7	0.4	1.30
1	40	FP	33	26.0	73.6	0.4	-
1	60	R	39	-	-	-	-
1	80	R	23	-	-	-	-
2	0	A	139	27.9	71.5	0.7	1.31
2	20	A	118	26.1	73.6	0.3	1.34
2	40	AC	75	25.9	73.7	0.4	1.36
2	55	FP	36	20.5	79.5	0.0	-
2	80	R	37	-	-	-	-
3	0	A	113	31.8	67.9	0.3	1.28
3	20	AC	68	32.1	67.8	0.1	1.31
3	30	FP	31	28.8	70.9	0.2	-
3	45	R	47	-	-	-	-
3	60	R	119	-	-	-	-
4	0	A	96	32.4	67.5	0.1	1.22
4	20	AC	62	31.7	68.1	0.2	1.32
4	40	FP	34	29.1	70.9	0.0	-
4	60	R	123	-	-	-	-
4	80	R	60	-	-	-	-
FP	FP-1	FP	20	-	-	-	-
FP	FP-2	FP	15	-	-	-	-
FP	FP-3	FP	15	-	-	-	-
FP	FP-4	FP	19	-	-	-	-

TABLE 3.3 SOIL and BEDROCK CHARACTERISTICS for SITE 3

Pit	Depth cm	Horizon	Ksat mm/hr	Clay %	Silt %	Sand %	Bulk
							density g/cm <sup>3</sup>
1	0	A	108	18.8	75.5	5.7	1.26
1	30	B	26	20.1	75.7	4.2	1.29
1	60	B	77	14.7	70.1	15.2	1.22
1	90	Bk	45	11.6	72.6	15.8	1.30
1	100	FP	14	-	-	-	-
2	0	A	73	19.6	78.0	2.4	1.41
2	30	B	25	15.3	76.2	8.4	1.35
2	60	B	23	19.6	80.3	0.2	1.44
2	90	FP	10	-	-	-	-
2	100	R	5	-	-	-	-
2	120	R	9	-	-	-	-
3	0	A	38	22.6	76.5	0.9	1.43
3	20	B	25	25.1	70.7	4.3	1.39
3	40	B	46	25.7	72.4	1.8	1.40
3	60	Bk	8	23.4	74.7	1.9	-
3	70	FP	4	-	-	-	-
3	90	R	6	-	-	-	-
4	0	A	59	24.1	75.1	0.9	1.24
4	30	B	31	16.9	76.0	7.1	1.34
4	60	Bk	53	15.1	78.8	6.1	1.36
4	90	FP	21	-	-	-	-
4	120	R	17	-	-	-	-
FP	FP-1	FP	14	-	-	-	-
FP	FP-2	FP	14	-	-	-	-
FP	FP-3	FP	18	-	-	-	-
FP	FP-4	FP	16	-	-	-	-